REPORT DOCUMENTATION PAGE

1. REPORT DATE (DD-MM-YYYY) 31-03-2008	2. REPORT TYPE Technical Report	3. DATES COVERED (From - To) 01-01-2007 – 31-12-2007

4. TITLE AND SUBTITLE
VKI Activities in Support of AFOSR Basic Research Interests

"Steady State Pyrolysis and Ablation Investigation"

5a. CONTRACT NUMBER

5b. GRANT NUMBER
FA9550-07-1-0089

5c. PROGRAM ELEMENT NUMBER

6. AUTHOR(S)
B. Vancrayenest, M. Playez, D. Fletcher

5d. PROJECT NUMBER

5e. TASK NUMBER

5f. WORK UNIT NUMBER
WP 2000

7. PERFORMING ORGANIZATION NAME(S) AND ADDRESS(ES)

von Karman Institute for Fluid Dynamics, Aeronautics and Aerospace Dept

Ch De Waterloo 72,
1640 Rhode-St-Genese
Belgium

8. PERFORMING ORGANIZATION REPORT NUMBER
VKI-CR-2008-29

9. SPONSORING / MONITORING AGENCY NAME(S) AND ADDRESS(ES)
USAF, AFRL
AF Off of Scientific Research
875 N. Randolph St.
Arlington VA 22203
USA

Kathryn P. Pheulpin
(703) 696-9735

10. SPONSOR/MONITOR'S ACRONYM(S)
AFOSR

11. SPONSOR/MONITOR'S REPORT NUMBER(S)
AFR LAFOSR-VA-TR-2016-0677
AFRL-AFOSR-VA-TR-2016-0677

12. DISTRIBUTION / AVAILABILITY STATEMENT
Unrestricted – A

Distribution statement A: Approved for public release. Distribution is unlimited

13. SUPPLEMENTARY NOTES

14. ABSTRACT
Compared to non-ablative materials, the stagnation point heat transfer process for ablators is extremely challenging to model, owing to the simultaneous presence of multiple material phases, and to strong diffusion and convection processes that occur from the material to the boundary layer. The objective of this work package is to develop the tools needed to perform careful, quantitative investigations of the interaction of pyrolysis gases with high temperature free stream gases representative of post-shock flow during atmospheric entry. The first part is on the development of quasi-steady state pyrolysis/ablation devices that provide steady pyrolysis or ablation conditions during which accurate species concentration measurements can be obtained using spectroscopic methods. The second part involves developing the spectroscopic measurement capability using a non-pyrolyzing ablative material, such as graphite. The third part is on application of spectroscopic analysis.

15. SUBJECT TERMS
Hypersonics, Ablation, Pyrolysis, Thermal Protection System, Emission Spectroscopy

16. SECURITY CLASSIFICATION OF:			17. LIMITATION OF ABSTRACT	18. NUMBER OF PAGES	19a. NAME OF RESPONSIBLE PERSON Dr. Olivier Chazot
a. REPORT open	b. ABSTRACT open	c. THIS PAGE open		43	19b. TELEPHONE NUMBER (include area code) 32 2 3599637

WP2000 - Part 1 Stagnation Point Heat Transfer With Gas Injection Cooling

1.1 Introduction

One type of thermal protection system, which is used by many capsules and probes, employs ablative composite material. At high temperatures the organic resin decomposes and vaporizes, absorbing some of the thermal energy; this process is known as pyrolysis. The pyrolysis gas is then injected into the flow creating a thin layer of cooled gas over the vehicle which blocks additional thermal load. The effect of blowing mass through porous walls, holes or slits has been studied in the literature but shows a large scattering of data. Related to the ablation re-entry flow regime, the convective blockage is the topic of this study. The release of pyrolysis gas will be simulated by injecting gas into the flow through multiple ports; this is known as transpiration cooling. The goal of this project is to investigate the reduction in heat flux caused by transpiration cooling for a probe in a subsonic plasma flow. Attempts will be made to correlate the change in heat flux to the mass flow rate and composition of the gas injected.

Extensive plasma tests were performed for different transpiration and plasma conditions. Different gases such as air, argon, and carbon dioxide were injected through the surface of the probe into the air plasma flow. The probes were also instrumented to measure temperatures, pressures, and heat flux within the probe. A significant part of this effort was focused on the development and verification of the gas injection system.

1.2 Facilities and testing

The Plasmatron is a high enthalpy facility in which a jet of plasma is generated in a test chamber kept at sub-atmospheric pressure (typically between 7 and

200 mbar). The plasma is generated by heating a gas (in the present study, only air plasma was considered) to temperatures up to about 10.000 K, using electrical current loops induced inside a 160 mm diameter plasma torch. The inductively-coupled plasma wind tunnel uses a high frequency, high power, high voltage (400 kHz, 1.2 MW, 2 kV) solid state (MOS technology) generator.

The accurate quantitative measurement of heat transfer rates in high enthalpy plasma facilities has always been a challenging task. Coupling gas injection systems with this type of measurement is even more difficult because of the need for the same space. The multi-point gas injection probe (Fig. 1.1) was based off the 14 mm diameter water-cooled calorimeter, which has been used successfully in the past at VKI to measure heat fluxes. In addition to measuring heat flux, this probe must inject gas uniformly into the plasma stream at the stagnation point for known conditions. The settling chamber for the gas had to be immediately after the front face; therefore, the water chamber could only be placed after the settling chamber. Thus, heat would is transferred by conduction through the copper side walls to the calorimeter. Since this heat conduction path from the front face to the water calorimeter has to be short and to allow for sufficient circulation in the water calorimeter, the volume of the gas settling chamber was significantly reduced (this raised concern over whether the injected gas would still be uniform across the front face. In order to assess the validity of this assumption, velocity profiles using hot wire velocimetry were performed latter and showed reasonable uniformity within 1 mm of the surface).
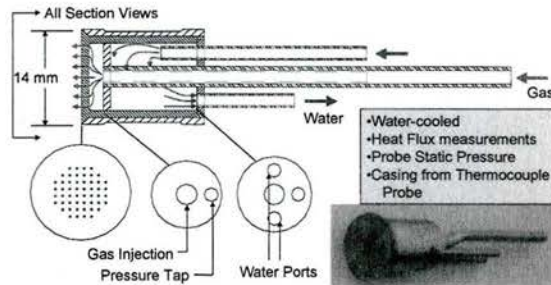

Figure 1.1: Steady-state water-cooled calorimeter with gas injection

In (Yakushin et al., 2001), different amounts of holes for the gas injection on the front face were tested: 21, 37, 57, and 77. The probe with 21 holes showed significantly less heat transfer efficiency compared to the others. There was little difference, however, between the 37 and 77 holes. Therefore, The 52 holes configuration was chosen, with a hole diameter of 0.3 mm (for a 2 mm gas injection pipe diameter) and a 1 mm distance between the holes, giving approximately a 2 hole diameter spacing between the holes.

A teflon piece is used to separate the probe from the holder. It limits heat flux loss due to conduction through the sidewalls, which are then considered

negligible. For the water calorimeter, conduction losses due to the proximity of the water inlet and outlet pipes must also be considered. The radiated heat flux of the cold-wall probe is also considered small, since the probe wall is kept at a low surface temperature. This effect was measured using a Gardon gage for air and CO_2 plasma at various static pressures. For the most extreme case, CO_2 at 70 mbar, maximum radiative loss was 5.4% of the total heat flux and represented, on average 4.6%.

The probe was inserted into the ESA sample holder, 50 mm diameter cylindrical blunt body. The gas was injected through a port in the back of the probe. The mass flow rate of the transpiration gas was measured using a G0-100 rotameter with a range of 0 to 1 g/s. The pressure transducer was located inside the arm of the model, so the gage pressure would be measured relative to the Plasmatron test chamber pressure. The mass flow of the cooling water is measured using a L16-630 rotameter. The pressure transducer for the pressure tap in the probe was an SM5415 with a 15 psi (1030 mbar) range. The rotameter for the transpiration gas was also switched after the initial tests. The G0-100 was used for the initial tests from 0.1 to 0.4 g/s. For measurements at a lower mass flow, the rotameter was switched to the L16-630 which has a range from 0 to 0.4 g/s.

1.3 Experimental results

Fig. 1.2 shows the heat flux measurements for air as the transpiration gas. The initial tests with the G0-100 rotameter were performed for the flow rates between 0.1 and 0.4 g/s. The results from these tests were as expected, as the transpiration mass flow rate was decreased the heat fluxed increased. Injected mass flow was found to be too high to study the region where the rise of heat flux is exponential as in (Yakushin et al., 2001), so the smaller rotameter was used to measure lower mass flow rates between 0 to 0.1 g/s. In Fig. 1.2, one can note differences in the two heat flux measurements at 0.1 g/s which can mostly be explained by this switch in rotameters. This difference will be discussed later in the uncertainties of the rotameter calibration.

The heat flux was found to unexpectedly decrease for low mass flow rates. The monotonic behavior observed in (Yakushin et al., 2001) was not reproduced. For all the power settings, the heat flux rises to a maximum heat flux at 0.04 g/s. For flow rates below 0.4 g/s, the heat flux decreases with decreasing transpiration flow rates, but then rises again somewhere between 0 and 0.01 g/s. Fig. 1.3 and 1.4 are the heat flux plots for carbon dioxide and argon (zero mass flow values in Fig.1.4 were obtained turning off the gas injection). They exhibit the same trend as air. The heat flux always reaches a maximum at 0.04 g/s.

1.4 Discussion of Results

Sensitivity studies for the injected gas pressure were performed in the transpiration gas rotameter and also for the static pressure in the test chamber. For
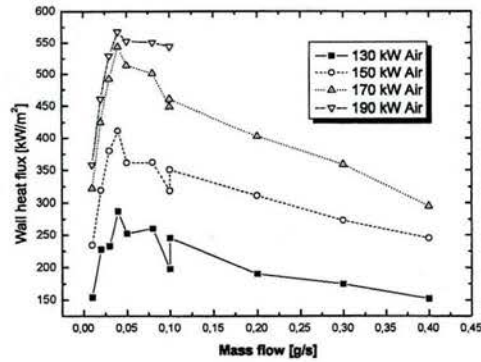
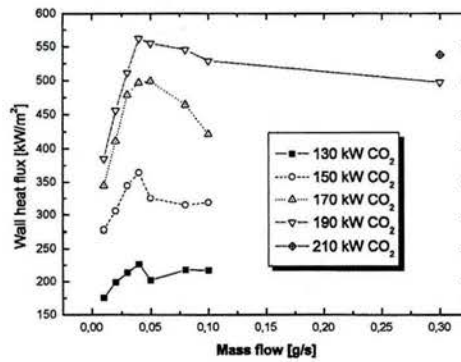Figure 1.2: Heat flux vs. transpirational $\dot{m}_{air}$

Figure 1.3: Heat flux vs. transpirational $\dot{m}_{CO_2}$

the last test case with nitrogen, a thermocouple was added to the gas injection pipe of the probe to determine whether the gas was getting preheated before reaching the settling chamber. The temperature measurements varied between 24 to 34ΣC, so its effect was determined to be negligible.

Pressure measurements inside the settling chamber of the probe were also made. These measurements were taken to determine the conditions of the gas before being injected. Unfortunately, the temperature of the gas could not be measured so that the gas in the settling chamber could not be completely characterized.
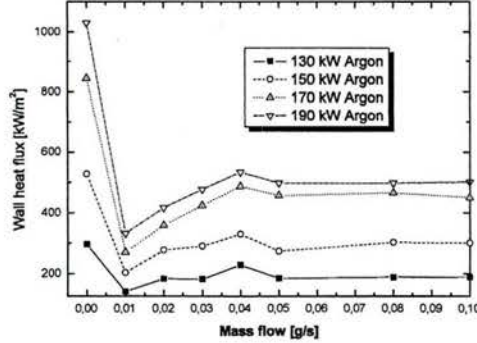
Figure 1.4: Heat flux vs. transpirational $\dot{m}_{argon}$

The pressure measurements could also be used to determine whether the velocity in the injection holes reached sonic flow using the following equation:

$$\frac{p_0}{p} = \left(1 + \frac{\gamma - 1}{2}M^2\right)^{\gamma(\gamma-1)} \tag{1.1}$$

where γ equals 1.4 for air, 1.29 for carbon dioxide, 1.4 for nitrogen, and 1.67 for argon. To check for the onset of sonic conditions, Mach number M, is set to 1. Even though the holes are choked, mass flow through the holes can still be increased because according to mass flow rate at a choked throat can be found by:

$$\dot{m}^* = \left(\frac{2}{\gamma + 1}\right)^{(\gamma+1)/[2(\gamma-1)]} \sqrt{\gamma/R}\frac{A^*P_0}{\sqrt{T_0}} \tag{1.2}$$

This equation shows that for a choked flow the mass flow rate is directly proportional to the throat area and the stagnation pressure and inversely proportional to the square root of the stagnation temperature. Therefore, if the stagnation pressure is increased the mass flow rate is increased. Choking seemed to be a possible cause for the unexpected heat flux measurements so the pressure ratios were increased by raising the test chamber static pressure to 200 mbar. Still the heat flux plot had the same trend. Therefore, possible sonic flow in the holes appears to not affect the trend in heat flux. Fig. 1.5 compares test chamber result for the static pressures of 200 mbar with nitrogen as the transpiration gas and 35 mbar for the other transpiration gases. The case for nitrogen at 35 mbar is not shown since a leak is suspected for this run. It should be similar to the other gases though, especially air which is 79% nitrogen.

The plots of the heat flux show three distinct regions. Although data points were not measured in the first region due to the limitations of the rotameter, heat flux was measured for mass flow rates of 0 and 0.01 g/s. From these two points, we can conclude that in general the heat flux decreases with increased transpiration mass flow within this range. For mass flows between 0.01 to 0.04 g/s, the heat flux rises with increased transpiration mass flow. For mass
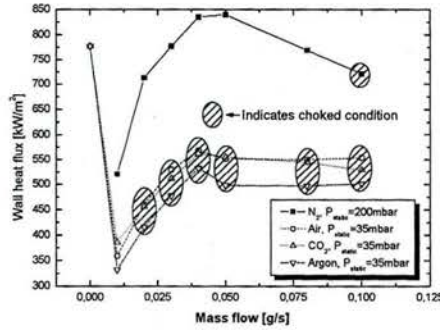
Figure 1.5: Heat flux with and without chocking

flows above 0.04 g/s, the heat flux becomes more constant, only slightly decreasing with increased transpiration mass flow. A reasonable explanation was established after a survey of film cooling (Bergeles et al., 1977) and a review of the videos from the tests.

Film cooling, typically for turbine blades, is similar to transpiration cooling in that gas is injected into the flow through many holes or slots. The difference is that film cooling is specifically for crossflows and generally intended to protect regions downstream of the flow. Still certain analogies can be made for transpiration and film cooling, and much more literature is available for film cooling.

For film cooling, there are two flow regimes: low and high injection rates. Injection rates are characterized by a blowing ratio M, defined as:

$$M = \frac{\rho_{gas} U_{gas}}{\rho_\infty U_\infty} \tag{1.3}$$

where, the $(\cdot)_{gas}$ subscript is for injected gas properties and the $(\cdot)_\infty$ subscript for freestream conditions. At low injection rates, the momentum of the impinging jet causes the injected gas to immediately bend along the surface of the probe. This creates a thin film over the surface which is very effective at cooling the surface. At high injection rates the jet penetrates into the mainstream and eventually separates from the wall. This is not as effective at cooling the surface.

For the case of film cooling, there exists an optimum blowing ratio, where the injected mass flux is high yet the jet remains attached to the wall. For example in Fig. 1.6 from (Bergeles et al., 1977), the optimum blowing ratio for this particular case was around 0.5. In this graph, η is defined as the wall film cooling effectiveness and x/D is a streamwise coordinate. We are not concerned with x/D for our study, but concentrating on one coordinate, you can see that effectiveness at first increases for higher blowing ratios then decreases after about 0.5.
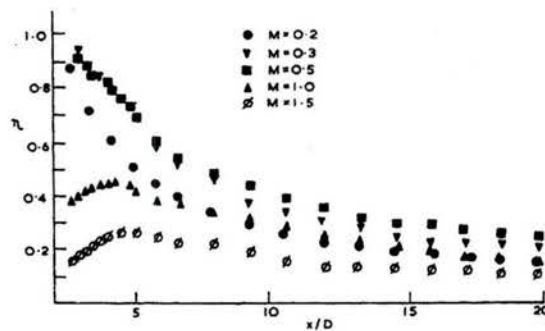
Figure 1.6: Effect of blowing ratio for film cooling

A similar situation could be argued for the current results. The dynamic pressure of the plasma jet at the location of the probe has been measured using a pitot probe and values are low (62.44 Pa for the 130 kW and 75.47 Pa for 150 kW). The velocities measured for the injected gas, on the other hand, were fairly large even in atmospheric conditions. Also, since the plasma jet is in a low pressure and high temperature condition the density of the gas is much lower. Ultimately, this leads to a high blowing ratio which means the transpiration flow could well be penetrating into the plasma jet. The carbon dioxide injection was shown to be an excellent tool for visualizing the transpiration flow and the carbon dioxide run videos support this hypothesis as seen in Fig. 1.7.

By dividing the mass flow rate of the transpiration gas by the area of the injected holes, the numerator of the blowing ratio can be determined. The denominator of the blowing ratio can be found using the dynamic pressure and plasma mass flow rate information. The blowing ratio M, for transpiration mass flow rate of 0.01 g/s and 0.10 g/s is approximately 3 and 30, respectively. Blowing ratios for the Mars Pathfinder were estimated according to results from a numerical study (Chen et al., 1995). Based on a given trajectory and heat shield made of silicone elastomeric charring ablator, known as SLA-561V, the maximum blowing ratio was approximately 0.01.

Although heat flux measurements were not taken at the low flow rates of the first region, there must be a steep decrease in heat flux with increasing mass flow, because the heat flux for zero mass flow is significantly larger than for 0.01 g/s. In this region, the transpiration gas encounters the impinging plasma jet causing a thin film of cool, transpiration gas to envelope the surface. This convective blockage shields the probe from the heat load, decreasing the heat flux the probe experiences. As the transpiration mass flow increases in this regime, the film becomes thicker and there is more mass to transport the heat load, so the heat flux continues to decrease.

For mass flows in the second regime, the jets from the transpiration probe are penetrating into the plasma jet. This is shown in Fig. 1.7, where the jets from the transpiration probe are creating a cone shape. This is a less effective heat shield because the transpiration gas is being used to cool a larger volume rather than a thin layer over the most critical region where heat transfer is the

highest. The transpiration gas is not as effective at cooling this larger volume, and it is the hotter gases in this recirculation region that are now in contact with the surface of the probe. As the injection rate is increased in this regime, the heat flux increases because the transpiration jets are penetrating further into the plasma jet increasing the volumes and becoming less effective.
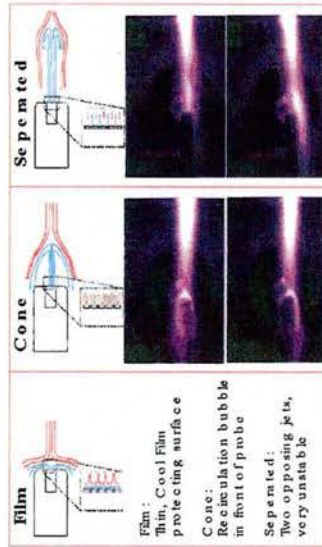

Figure 1.7: Three flow regimes

In the third regime, the jets of transpiration gas have penetrated so far into the plasma jet that the cone has become detached. A region covering the probe surface is no longer defined. Instead, the transpiration gas is a jet in front of the probe. Heat from the plasma flow can come in direct contact with the surface due to instabilities in the opposing jets. Increases in injection rates decrease heat flux only slightly since the additional mass is less effective so far away from the probe surface.

The results from (Yakushin et al., 2001) showed an exponential decrease in heat flux with increasing mass flow rates. This would correspond to the results expected for the first regime. Unfortunately, we were not able to achieve blowing ratios that low.

1.5   Heat flux measurement uncertainties

To calculate the heat flux the probe experiences the following energy balance, as discussed previously, is applied:

$$q_w = \frac{\dot{m} \cdot Cp \cdot (T_{out} - T_{in})}{A} \qquad (1.4)$$

Therefore, the uncertainties in the heat flux measurements arise for a combination of the uncertainties in the measurement chain with:

- $\dot{m}$ is the mass flow rate of the water through the calorimeter, measured with a ROTA L16/630-6404. Uncertainty of mass flow rate will typically be $\delta(\dot{m}) = 1/50 = \pm 0.02$ g.

- Cp is the specific heat of water. For the range of temperatures the water experiences, the change in Cp was estimated to be $\delta(Cp) = 0.01$ J/kg-K.

- T_{out} and T_{in}, are the temperatures at the outlet and inlet of the calorimeter. The temperatures are measured using thermocouples.

- A, is the area of the sensing element. The diameter of the face is 14 mm and uncertainty in the diameter is estimated to be ± 0.1 mm. $\delta(T_{read,in}) = \pm 0.3$ ΣC, uncertainty in temperature going into the calorimeter. $\delta(T_{read,out}) = \pm 0.7$ ΣC, uncertainty in temperature leaving the calorimeter.

The most probable error in a measurement can be calculated using the following equation:

$$\left(\frac{\delta q}{q}\right)^2 = \left(\frac{\delta \dot{m}}{\dot{m}}\right)^2 + \left(\frac{\delta Cp}{Cp}\right)^2 + \left(\frac{\delta A}{A}\right)^2 \\ + \left(\frac{\delta T_{in}}{\Delta T}\right)^2 + \left(\frac{\delta T_{out}}{\Delta T}\right)^2$$

(1.5)

where ΔT is the temperature difference between $T_{out} - T_{in}$.

Table 1.1: Breakdown of heat flux uncertainties.

Breakdown of Uncertainties						
Percentage of Uncertainty/Total Heat flux						
Run	$\dot{m}_w$	Cp_w	A	T_{out}	T_{in}	total
Air	1,8	0,2	1,4	6,9	2,9	13,3
CO2	1,5	0,2	1,4	7,5	3,2	13,8
Argon	2	0,2	1,4	6,3	2,7	12,6
Combined	1,7	0,2	1,4	6,9	2,9	13,2

Table 1.1 shows a breakdown of the uncertainties. For each test condition, the uncertainties were calculated then divided by the total heat flux measured to obtain a percentage. These percentages were then averaged for the different gases tested. The last row shows the average of the three runs. The temperature measurements are the largest source of error, because the fluctuations in the temperature make it difficult to determine the steady state value. The last column shows the total uncertainty for the measured heat flux.

1.6 Improvements and further studies

In order to be able to perform measurements in the first transpiration film cooling regime which is more representative of ablating re-entry flight conditions, the easiest way to proceed is to decrease the transpiration mass flow. Adaptations

to the existing setup are currently in progress. Another way to measure this first regime accurately without having to go to lower transpiration mass flow rates would be to decrease the blowing ratio but working conditions affecting this ratio are more uncertain.

As mentioned previously in the probe design section, the heat flux measured is only relative to the front face, because there is a cool layer of gas in between the majority of the area between the front face and the calorimeter. The heat is primarily transferred to the calorimeter through the cooper walls. Heat pipes could be implemented but one can imagine that the best option for the next generation of combined transpiration/heat flux probe is to eliminate the settling chamber behind the front face and make it coaxial with the heat flux sensor. The front face and the water/slug calorimeter could be made of the same block. The front face could be made thicker so that ducts can be machined into it to feed the injection holes. In this way, the calorimeter would be covered by a thicker that will create the settling chamber for the injected gas.

1.7 Conclusions

The goal of this study was to gain experience in transpiration cooling in a subsonic plasma stream. This was achieved by a multistage design and test approach. The probes were able to inject gas uniformly into the plasma flow. This was verified by measuring the velocity profiles of the injected gas. The probes successfully measured conditions of the gas (temperature, pressure, and heat flux) before being injected into the flow. Relationships were then developed and verified for various plasma conditions, transpiration gases and mass flow rates in the Plasmatron facility.

Some of these results were unexpected. However they do appear to be consistent with other research on film cooling. Through this investigation, it was determined that the tests were performed at higher blowing ratios than expected, and the transpiration gas was actually penetrating the plasma jet. Recommendations were made for improvements and verification of the three flow regimes assumption.

New probe designs for the Plasmatron facility are never straightforward. By taking a multistage approach, though, we have successfully gained experience in transpiration cooling in a subsonic plasma flow. Eventually, this probe and knowledge will be applied to ablation research for a better understanding of pyrolysis gas injection.

Bibliography

G. G. Bergeles, A. D. Gosman, and B. E. Launder. Near-field character of a jet discharge through a wall at 30 degrees to a maintream. *AIAA journal*, 15(4): 499–504, 1977.

Y. K. Chen, W. D. Henline, and M. E. Tauber. Mars Pathfinder trajectory based heating and ablation calculations. *Journal of Spacecraft and Rockets*, 32(2):225–230, March-April 1995.

M. I. Yakushin, I. S. Pershin, and A. F. Kolesnikov. An experimental study of stagnation point heat transfer from high-enthalpy reacting gas flow to surface with catalysis and gas injection. In *Proceedings of the fourth European Symposium on Aerothermodynamics for Space Vehicles*, pages 473–479, Capua, Italy, 15 - 18 October 2001.

WP2000 - Part 2 Emission spectroscopy analysis of ablating graphite

1.1 Introduction

During the mid-fifties, because of new needs créated by the appearing mid/long range ballistic missiles, and the newly emerging space missions, ablative materials proved to be valuable solutions for thermal protection systems of space vehicles travelling in the hypersonic flight regime[1]. The Apollo program, with the Moon landing in 1969, probably represented the apogee of interest in the development of ablators. In October 1968, NASA began early studies of space shuttle designs and most of efforts turned toward non ablating reusable materials for more than two decades. Nowadays, the outer planets missions require the development and refinement of thermal protection system materials for very high entry velocities. One can also anticipate that the size reduction of the Orbiter successor will lead to an increase in term of heat fluxes, hardly compatible with the reusable heatshield concept, already mauled with the conditions encountered by the actual lifting body vehicle. Ablation experiences a new lease of interest.

Although ablators have been extensively used in the past, the underlying physics is still poorly elucidated. For many problems like roughness induced transition, liquid layer behavior or thermomechanical effects (swelling, expansion and cracking of pyrolysable materials), black box models are used, based on wind tunnel and plasma jet experiments. In particular, interactions between outgassing species coming from the in-depth decomposition of the organic resin (in the case of pyrolysable materials), carbon species coming from the surface consumption and the freestream flow surrounding the reentry vehicle are extremely complex within the ablation layer, because of the multiplicity of physical phenomena involved and their potential non-linearities.

Pyrolyse and ablation are efficient processes for aerothermal heat load rejection, and are combined in the use of charring ablator. But the internal decomposition of the solid organic resin (composed of C, H and O) releases

1

complex hydrocarbon gaseous species within the ablation layer. In 2002, the von Karman Institute for Fluid Dynamics (VKI) initiated a study related to the interaction of ablation products and outgassing species with the plasma flow. As a first step, and in order to restrict the number of candidate species in the flow, decision was taken to consider only ablation, that is a combination of processes that consume the heat shield material. The photochemistry of plasma is being investigated with a simple ablatable material, namely graphite. First attempts were conducted in the Minitorch inductively coupled plasma facility at modest enthalpy conditions. These initial experiments of this investigation were presented and discussed in [2]. The ablating material testing and spectral data acquisition were successfully integrated, providing emission spectra of graphite ablation in both nitrogen and air plasmas. But these first test results showed the limited capability of the Minitorch for ablation studies; and the necessary move to the Plasmatron, with a greater enthalpy range.

Graphite has been used extensively as a heat shield material because it has good high temperature behavior and provides a high emittance surface. Study of aerothermal behavior of graphite also aids in understanding the behavior of carbonaceous surfaces during ablation: in most cases, remnant of charring ablators can be considered as pure carbon. Ablation of graphite on atmospheric reentry continues to be actively studied to reach greater fidelity of simulation and to support new concepts for CFD calculations. Material properties have been extensively studied and minimize uncertainties from material properties. Despite the maturity of the field (key studies date to at least 1965), models for the surface chemistry differ from study to study. Concerning experimental ablation studies in the open literature, only a few were reported with sufficient detail to be reproduced. The more extensive efforts were those obtained during the PAssive Nosetip Technology (PANT) program. Major results were stagnation point recession rates, stagnation point pressures et stagnation point temperatures for blunt bodies of 12.7 mm. Lundell and Dickey [3] also gave stagnation point surface temperature, pressure and recession rates in the Ames arc heated wind tunnel. But they failed to give adequate freestream conditions such as velocity, temperature and species concentration. But the principal shortcoming of the work is the paucity of experiment for stagnation pressures below 80 atm (except the noticeable contribution of Wakefield[4] at 0.06, 0.1 and 0.3 atm in an airstream). So the primary goal of the present study is to provide a coherent set of data at low pressure (50 to 200 hPa) including information on near surface spectroscopy and surface temperature, as well as freestream characterization: fully catalytic cold wall heat flux, stagnation pressure, velocity and enthalpy. The final goal is to support the actual need for code validation. In the following sections description of the facility and instrumentation are given. They are followed by a presentation of preliminary results and perspectives for future work.

1.2 Experimental facility and test conditions

1.2.1 Plasma torch description

The Plasmatron, presented in figure 1.1(a), is a high enthalpy facility in which a jet of plasma is generated in a test chamber kept at sub-atmospheric pressure

2

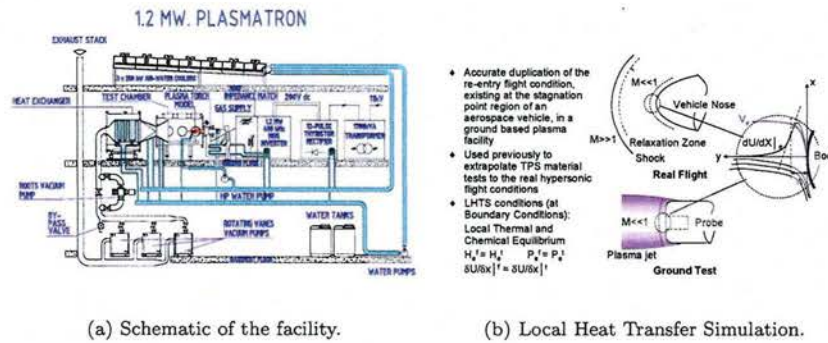(a) Schematic of the facility.   (b) Local Heat Transfer Simulation.

Figure 1.1: Inductively Coupled Plasma Facility.

(typically between 7 and 200 mbar). The plasma is generated by heating a gas to temperatures up to about 10.000 K, using electrical current loops induced inside a 160 mm diameter plasma torch. The inductively-coupled plasma wind tunnel uses a high frequency, high power, high voltage (400 kHz, 1.2 MW, 2 kV) solid state (MOS technology) generator. To the authors' knowledge, most of properties and characteristics of ablators are obtained from three sources: arc heated wind tunnels, ballistic range tunnels and flight tests. Ballistic range tunnels are difficult to exploit for spectroscopic studies for obvious reasons, and the cost of real flight is prohibitive. Arc heated wind tunnels are good at reproducing realistic enthalpy levels, and may also reproduce Mach numbers under certain circumstances. But the flow that they produce is usually not uniform, and not in thermal or chemical equilibrium: the freestream flowfield is not easily characterized. Metallic contaminants coming from the electrodes may also interfere with the ablation test during the spectroscopic survey. Those difficulties are usually overcome using Inductively Coupled Plasma (ICP) facilities like the Minitorch or the Plasmatron. They are operated in subsonic mode, where it is more likely to produce conditions in the stream that are near thermal and chemical equilibrium. In the absence of electrode and associate erosion, the chemical purity of the freestream is also supposed to be improved. The TPS testing methodology at VKI is based on Local Heat Transfer Simulation (LHTS) shown in figure 1.1(b). This approach, which relies on a duplication of the stagnation point re-entry conditions in a Plasmatron facility[5], allows the evaluation of the interaction of the TPS material and the surrounding high temperature flow.

As previously explained, ICP wind tunnels are very appropriate tools to alleviate the paucity of experiment for stagnation pressures below 80 atm, and particularly to study low pressure effects on thermochemical non equilibrium around the test article. For this reason, six different conditions were selected: static pressures equal to 50, 100 and 200 hPa (respectively 37.5, 75 and 150 torr), for nitrogen and air plasmas, and constant anode power. Test conditions are summarized in table 1.1.

3

Table 1.1: Plasma torch working conditions.

Test	Atmosphere	Anode power $[kW]$	Static pressure $[hPa]$	Mass flow $[g/s]$
POCO3	Air	150.	50.0	16.
POCO5	Air	150.	100.0	16.
POCO4	Air	150.	200.0	16.
POCO6	N_2	150.	50.0	16.
POCO7	N_2	225.	50.0	16.
POCO8	N_2	225.	200.0	16.
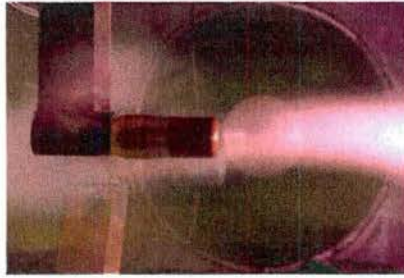
(a) Combined probe for dynamic pressure and cold wall heat flux determination. Sample-holder for ablation testing is visible in the background.
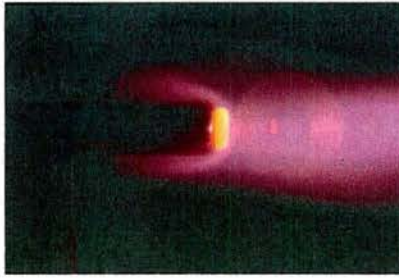
(b) Ablation test of graphite (42 mm diameter model).

Figure 1.2: Multiple probe injection capabilities.

1.2.2 Freestream characterization

The VKI Plasmatron now offers multiple probe injection capabilities, allowing freestream conditions characterization during the same run as ablation tests. Intrusive measurements are performed before and after sample-holder injection to assess steady-state working conditions in the test chamber. Dynamic pressures and fully catalytic cold wall (FCCW) heat fluxes are measured using a steady-state (water-cooled) calorimeter included in a combined probe shown in figure 1.2(a). Experimental data are given for each test condition is table 1.2. The external geometry of the probe is based on the standard 50 mm diameter ESA model. Freestream enthalpy and velocity are obtained using a VKI in-house numerical code, introducing measurements of cold wall temperature, fully catalytic heating rates, stagnation and dynamic pressures.

One important issue still need further investigations: because of the 4 mm protrusion of the sample, the external geometry of the test article is slightly modified, as well as velocity gradients, thus changing the heat transfer rate to the sample surface compared to the FCCW measurement presented above. The increase is difficult to estimate a priori since the change of effective radius radius is not well known. In hypersonic, in the particular case of a hemispherical nose, the velocity gradient can be evaluated from Newtonian flow[6]. For a family of sharp-cornered blunt axisymmetric noses on cylinders, it has been

4

Table 1.2: Freestream conditions.

Test	FCCW heat flux [W/cm^2]	Dynamic pressure [Pa]	Enthalpy [MJ/kg]	Velocity [m/s]
POCO3	82.8	37.	15.7	168.
POCO5	66.7	14.	13.6	71.
POCO4	52.4	8.	10.5	35.
POCO6	59.7	23.	X.	X.
POCO7	147.0	49.	X.	X.
POCO8	69.9	8.	X.	X.

determined experimentally. Unfortunately, no equivalent study was performed in the subsonic regime, and the effects of corner radius on stagnation-point velocity gradients on blunt axisymmetric bodies do not exist as they are in the hypersonic regime[7]. The use of slug calorimeters mimicking the exact sample geometry may be one way to correctly estimate this increase of hear transfer rate and should be experimentally investigated. CFD tools may also be of great help.

One can also note that dynamic pressures recorded during the runs, and as a consequence, freestream velocities given by the rebuilding code[8] are suspiciously low. Since repeatability from one run to another was shown to be reasonably good in the previous experimental campaigns, new measurements will be performed to assess the validity of the present results.

1.2.3 Surface temperature measurements

Consecutively to its injection into the plasma jet, the test piece becomes surface reacting because of the rise of its surface temperature. This parameter is the key one to determine physical phenomena driving the ablation process. Scala and Gilbert identified the different mass transfer regimes for ablating graphite[9]. These are presented in figure 1.3. In the present study, the surface temperatures are in the range 1200 °C-2200 °C and pressures are moderate, comprised between 50 and 200 hPa. Graphite ablation will be primarily the result of diffusion controlled oxidation and no sublimation occurs.

For material testing, as the years go by, two-color pyrometry stands out as one of the most convenient and reliable surface temperature measurement technique implemented within plasma wind tunnels. Two models of pyrometers are currently used at VKI depending of the temperature to be monitored: a Raytek Marathon MR1S-B (temperature range from 700 to 1800 °C) and a Raytek Marathon MR1S-C (temperature range from 1000 to 3000 °C). The fundamental working hypothesis of this type of device is the existence of a gray body behavior (constant spectral emissivity over the wavelength of interest). In the present case, the two monochromatic luminances are respectively evaluated at 0.95 and 1.05 microns. According to literature[10, 11], most of graphites fulfill this condition. Since in situ calibration is difficult in the wind tunnel at high temperatures, and assessment with back face tungsten/rhenium thermocouples may be disturbed by potential conductive losses and 2D configuration problems, decision was taken to make technique-to-technique comparison with infrared thermography (in the range 8-9 μm) and blackbody radiation (in the
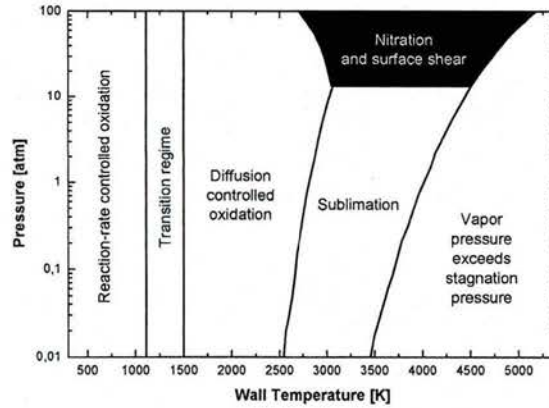
Figure 1.3: Mass transfer regimes for ablating graphite, depending on pressure and surface temperature.

VIS-NIR region) to check the consistency of our working hypothesis. Figure 1.4 shows a record of IR thermography using a FLIR Thermacam SC3000, working between 8 and 9 μm in the range of ambient conditions up to 1500 °C for varying conditions with time. We assumed a constant spectral emissivity value equal to 0.85 and an angle of view equal to 45 °, leading to an effective emissivity of 0.6. For the various working conditions, reasonable agreement was found with 2-color pyrometry up to 1300 °C. From this threshold temperature, important discrepancies appear with numerous potential sources. Surface temperature measurement was also done recording VIS-NIR radiation emanating from the surface of the ablating test piece using emission spectroscopy setup detailed latter in this report. Figure 1.4(b) clearly shows superposition of the following spectral features: radiation emanating from the boundary layer is composed of overlapping bands of CN violet and N_2^+ in the range 350-450 nm plus a peak of atomic oxygen at 777 nm. In the range 450-760 nm, the Planck emission is the dominant contribution. A non-linear least-squares routine was implemented using surface temperature and total emissivity as free parameters for the Planck distribution function. The surface temperature was found to be equal to 1341$\pm$3 °C while the pyrometer gave a surface temperature equal to 1370 °C. Therefore, the agreement between the three different techniques, working in three independent spectral regions (450-760 nm, 950-1050 nm and 8000-9000 nm) is found to be good enough to consider the real-time monitoring by pyrometry as a reliable measurement technique. Care should be taken in case of other material with slightly different optical behavior, or pyrolysing materials which may inject emitting/absorbing species within the ablation layer, similarly to what happens within the shock layer[12].

1.2.4 Experimental set-up for emission spectroscopy

Emission measurements are the simplest optically based non-intrusive diagnostics that can be used in high-enthalpy plasma facilities. Thermal excitation

6
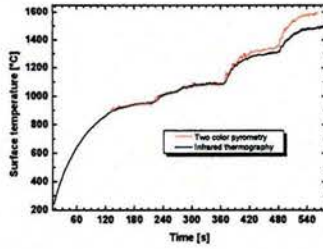
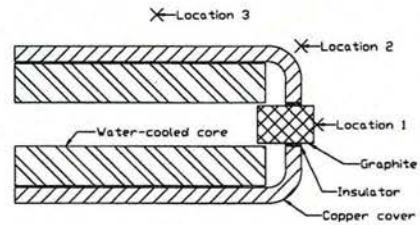(a) Temperature monitoring and comparison pyrometer/infrared camera.
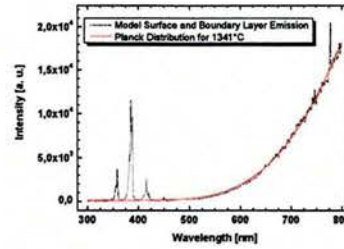
(b) Planck distribution function.

Figure 1.4: Technique to technique comparison for surface temperature measurement.

(a) Experimental set-up: collecting optics, displacement table, sample holder and ICP torch

(b) Locations of emission survey

Figure 1.5: Optical set-up at the Plasmatron facility.

within the observed flow region continuously replenishes populations in radiating electronic levels. For applications of emission spectroscopy to flow property measurement in facilities that simulate atmospheric entry, the wavelength range of interest covers the region from the UV to the IR. Instrumentation for emission spectroscopy is comprised of three main elements: a light collection system, a spectrograph or monochromator and a photo detector.

The light emitted from the plasma is collected by a 50.8 mm diameter, 500 mm focal length spherical mirror to prevent chromatic aberrations. After reflection on a flat mirror, the plasma flow is imaged on a 600 microns core diameter fiber. In order to reduce stray light and improve spatial resolution, an aperture is put in between, for a target f-number equal to 50. The spectrometer was an Ocean Optics model HR2000CG-UV-NIR, equipped with a fixed, holographic grating (300 grooves/mm), a 5 microns entrance slit and a 2048-element linear silicon CCD array. It offers the possibility to obtain rapidly low resolution spectra on the nominal bandpass from 200 to 1100 nm, allowing quick analysis and identification of present radiating species. The apparatus function resulting from the association of the slit, the grating and the detector element size was measured observing the diffracted light of an HeNe laser at 632.8 nm. The Full Width at Half Maximum (FWHM) was found equal to 1.1 nm. The fixed grating provides high acquisition rate and time-resolved spectroscopy, ideal for recessing surface and ablative material testing. The light collection system is mounted of a X-Y displacement system shown in figure 1.5(a), allowing multiple measurement locations shown in figure 1.5(b). As a reference, the position 1 is located on the centerline of the sample and the plasma jet, 447 mm from the torch exit.

Calibration of the whole system, including the light collection system and spectrometer efficiencies was performed (figure 1.6) to provide absolute measurements using a reference tungsten ribbon lamp (OSRAM-WI17G). Below 350 nm, the emission of the lamp is too weak to allow an accurate measurement, thus limiting the usable spectral range. The same way, the upper limit was determined to be 900 nm. Hopefully, most spectral features of interest are comprised in the range 350-900 nm, except the 4th positive system of CO, of interest because of the oxidation process and known to be a strong radiative species in the UV region. NO is also known to have a significant contribution in the UV region, and would be of interest to determine the translational temperature [13].

Since the technique is based on line-of-sight measurements along several chords of the plasma ahead of the sample holder. For this reason, emission spectroscopy is not spatially resolved. Under the assumption of flow axisymmetry and narrow probed volume (ideally pencil-like), local values could be inferred applying classical Abel-inversion routines. Nethertheless, scanning the circular cross sections leads to long duration tests that are not easily compatible with recessing surfaces of ablating materials. This issue will have to be investigated more in the future.
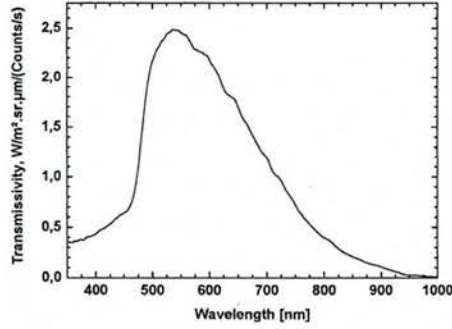
Figure 1.6: Calibration of the measurement chain.

Table 1.3: Surface temperature, pre- and posttest evaluation.

Test	Duration [s]	Initial mass [g]	Mass loss rate [g/s]	Recession rate [mm/s]	Mean surface temperature [°C]
POCO3	378.	3.688	3.968E-3	1.71E-3	1485.
POCO5	403.	3.699	3.300E-3	1.54E-3	1330.
POCO4	420.	3.719	3.595E-3	1.59E-3	1290.
POCO6	720.	3.693	2.778E-5	9.03E-5	1245.
POCO7	940.	3.684	2.128E-5	1.44E-4	1970.
POCO8	690.	3.648	1.449E-5	1.00E-4	1405.

1.3 Results and discussion

1.3.1 Surface temperature, surface state, global recession and mass loss rates

The test piece consists in a 18 mm long, 12 mm, sharp edged cylinder with polished surface. Only 4 out of the 18 mm were exposed to the flow in order to limit the influence of the sample presence on the velocity gradient around the test article. The rest of the cylinder was inserted inside the sample holder, held in place by three insulating pins. A virgin sample is shown in figure 1.7(a).

Surface temperatures are recorded using the Marathon MR1S-B already mentioned earlier, masses are measured using a Kern EW150-3M 1 mg precision balance, and lengths using a 0.01 mm precision caliper rule. Initial masses, mass loss rates, recession rates and mean surface temperatures are given in table 1.3 for each run.

Tests in air were conducted at thee different static pressures (50, 100 and 200 hPa) at constant anode power (150 kW). In the 50 hPa case, surface remains apparently flat and parallel to the initial one despite the recession (figure 1.7(b)). It also presents a uniform arrangement of very small asperities. Sharp edges were consumed and are no longer visible. In the 200 hPa case, surface consumption rounded off the edges and the surface at the same time (figure 1.7(c)). Rough elements are clearly visible. The case at 100 hPa is not presented since the

9

surface state and recession are intermediate. Surface temperature is decreasing with increasing static pressure (thus decreasing freestream enthalpy). Despites the different resulting geometries, mass loss rates and recession rates are of the same order (respectively about 3.5 mg/s and 1.6 μm/s) for the three cases.

No similar behavior was observed in nitrogen atmosphere. The 50 hPa/150 kW anode power case presents no significant mass loss or recession (both are about two orders of magnitude lower than in the case of air). Surface was found to be slightly dark and unpolished (figure 1.7(d)). Decision was taken to investigate at higher enthalpy level (225 kW anode power) for two different static pressures (50 and 200 hPa). In the 50 hPa/225 kW case, global recession and mass loss were not significantly higher, but a thin black coating is clearly visible (figure 1.7(e)) on top of the virgin surface. Edges also present signs of chemical activity. In the last case (200 hPa/225 kW), global mass loss and recession rates are of the same order of magnitude, the surface is very dark and unpolished and edges are slightly rounded (figure 1.7(f)). Evidence of carbon redeposition on the surface are present in the three different cases. The layer was very thin and fragile for POCO6, to a lesser extend for POCO8 and relatively thick and persistent for POCO7.

1.3.2 Experimental spectra

A key issue in an ablation study in to include all relevant chemical species. They are introduced by the initial freestream species, the gaseous species injected by the ablator and the interaction between the flowfield species and the injected species. For air, the initial species are N_2 and O_2. As the flow passes through the shock wave surrounding the body, additional species are produced by dissociation and exchange reactions: N, O and NO. Finally the species injected by the ablator must also be considered: because oxidation of the graphitic surface is the only mechanism allowed at the surface, only CO is considered[14]. Sublimation products (among them C, C_2 and C_3 are the dominant species) do not have to be included in our case. Finally, species are also produced through interaction between the flowfield and injected species: CN and CO_2. Therefore, the relevant species are: N_2, N_2^+, CN, O and N. Radiation of O_2, NO and CO is important in the UV region, but below the spectral range of the present study.

Air Atmosphere

All spectra presented have been normalized for the relative spectral response of the optics and detector using a calibrated tungsten standard lamp. Generally, the emission spectrum at the subsonic air flows typically investigated in the described facility are dominated by the emission of the molecules NO, N_2 and N_2^+ in the UV region, and by molecular emission of N_2 and atomic oxygen and nitrogen in the visible to the near infrared wavelength region. The experimental spectrum shown in figure 1.8(a) was recorded in an airstream (POCO4 conditions) prior to the probe injection. As expected, it contains a wealth of emission features. The second positive system of N_2 (transition $C^3\Pi_u - B^3\Pi_g$) is not clearly visible. The $\Delta\nu = 0$ sequence is located at 337 nm and the system extends from 310 to 465 nm. The main radiating species between 350 and 450 nm is the first negative system of N_2^+ (transition $B^2\Sigma_u^+ - X^2\Sigma_g^+$). The 0-0 band is located at 391 nm. The free features located between 600 and 900 nm
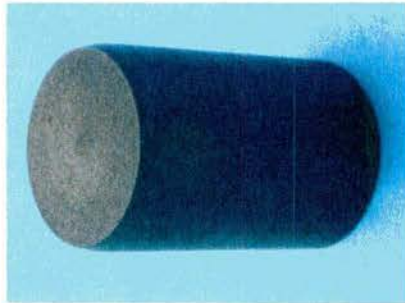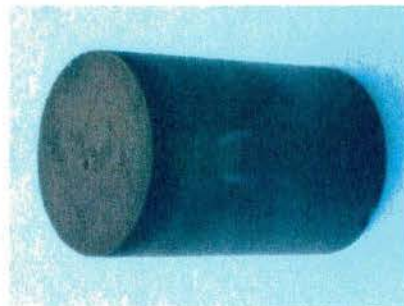
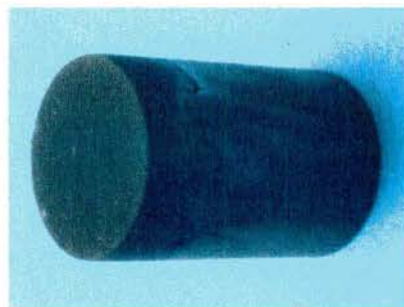(a) Virgin sample
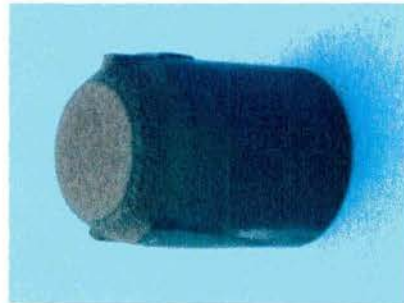
(b) Posttest POCO3
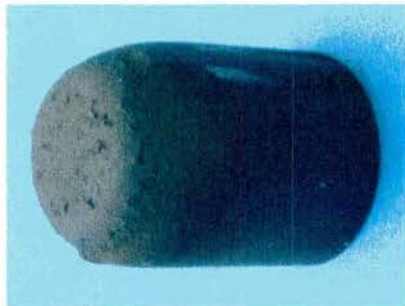
(c) Posttest POCO4

(d) Posttest POCO6

(e) Posttest POCO7

(f) Posttest POCO8

Figure 1.7: Pre- and posttest photos of POCO samples.

correspond to the first positive system of N$_2$ (transition $B^3\Pi_g - A^3\Sigma_u^+$). The 777 nm feature is assignable to atomic oxygen (transition $^5P -^5 S$) as well at the 844 nm (transition $^3P -^3 S$). There is no evidence of atomic transition of N, since the usual 742, 744 and 746 nm features were not observed.

Spectrum presented in figure 1.8(b) was recorded ahead of a water-cooled copper surface (position 1). It presents the same radiating species at lower intensities, plus some additional atomic features in the NIR region. The atomic transitions of nitrogen, at 742, 744 and 746 nm are clearly visible.

Figure 1.8(c) presents the experimental spectrum recorded ahead of ablating graphite. The CN violet system (transition $B^2\Sigma^+ - X^2\Sigma^+$) dominates the spectrum, with a maximum close to 388 nm ($\Delta\nu = 0$) and high intensities for sequences $\Delta\nu = \pm 1$. For higher wavelengths, the spectrum is dominated by the CN red system (transition $A^2\Pi - X^2\Sigma^+$). Even if the peak of this system is around 1100 nm for the $\Delta\nu = 0$ sequence, CN red dominates the spectrum down to 600 nm. Sequences from $\Delta\nu = +2$ to $\Delta\nu = +5$ are visible in figure 1.8(d). No evidence of C$_2$, especially the C$_2$ Swan system (transition $d^3\Pi_g - a^3\Pi_u$) with its $\Delta\nu = 0$ sequence located at 516 nm, was observed. The peak at 589 nm is assignable to sodium D-line emission and may indicate possible presence of water in the compression station (atmospheric air is used), or impurities in the graphite. The oxygen triplet located at 777 nm is also visible.

Influence of graphite ablation is still visible at position 2. Even if the spectrum shown in figure 1.8(e) is very similar to the one recorded in the freestream from wavelengths comprised between 450 and 900 nm, the CN violet system is the dominant radiating species over the range from 350 to 450 nm. 50 mm downstream (position 3,) no influence was seen. Spectral features are similar to the ones present in the freestream and are weaker due to the presence of the water-cooled sample holder within the plasma flow (figure 1.8(f)).

Nitrogen Atmosphere

The interest of pure nitrogen as test gas lies in the limited number of relevant species compared to air, since NO, O, O$_2$, CO and CO$_2$ are excluded from the study. As expected, in the freestream prior to probe injection, the emission spectrum shown in figure 1.9(a) presents the same molecular features of N$_2$ and N$_2^+$ previously mentioned. The $\Delta\nu = -2$ sequence of N$_2^+$ first negative is clearly visible around 450 nm. The same comparison can be done in front of the water-cooled calorimeter: as shown in figure 1.9(b), molecular features of N$_2$ second positive and N$_2^+$ first negative were identified, as well as transitions of N atoms in the NIR portion of the spectrum.

Figure 1.9(c) shows an emission spectrum recorded in front of the hot eroding sample. The increase of intensity in the 350-450 nm region is attributed to the presence of CN violet, resulting from chemical reactions in the near surface region between of the nitrogen plasma and the ablating graphite. Overlapping sequences $\Delta\nu = +1, 0, -1, -2$ of CN violet and N$_2^+$ first neg are observed: the N$_2^+$ and CN molecules are isoelectronic, making their spectra very similar. Figure 1.9(d) presents typical CN red emission in the range 600-900 nm. As in air, atomic peak of sodium was observed at 589 nm: we have confirmation that sodium comes from impurities present in the graphite test piece.
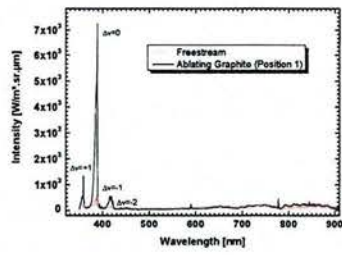
Measured spectra at position 2 (figure 1.9(e)) do not show any presence of CN. It tends to confirm the fact that chemical reactions occurring between the
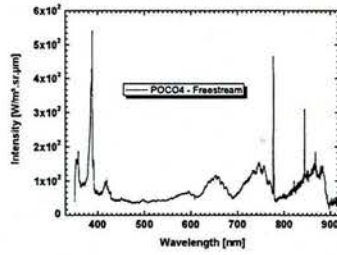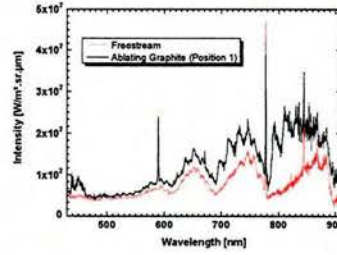
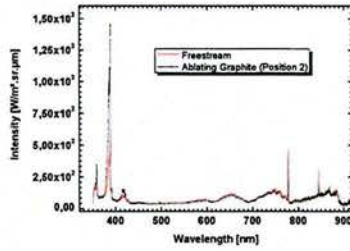(a) Emission spectrum of the airstream.
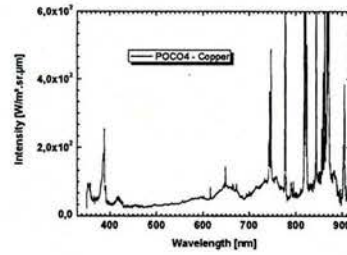
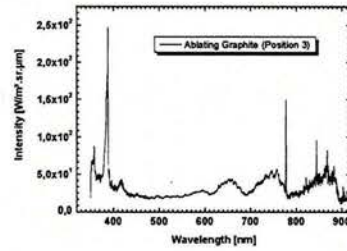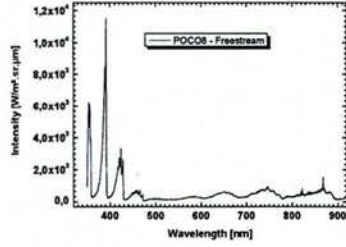(b) Emission spectrum ahead of water-cooled copper surface.

(c) Emission spectrum ahead of ablating graphite.

(d) Emission spectrum ahead of ablating graphite (detail).

(e) Emission spectrum ahead of ablating graphite.

(f) Emission spectrum ahead of ablating graphite.

Figure 1.8: Experimental emission spectra in air (condition POCO4).

13

nitrogen plasma and the surface are in a very limited zone. Carbon species are not carried away, and this result is in agreement with the negligible mass loss and recession rates observed. 50 mm downstream (position 3,) no influence was seen. Spectral features are similar to the ones present in the freestream and are weaker due to the presence of the water-cooled sample holder within the plasma flow (figure 1.9(f)).

1.4 Summary and perspectives

All the first demonstration experiments have proved the viability of the concepts used. The ablating material testing and spectral data acquisition were successfully integrated, providing emission spectra of graphite ablation in nitrogen and air plasmas at low pressure. Special care was given to the ablating environment characterization: $\dot{q}_{FCCW}$, T_{wall}, P_∞, P_{dyn}. Some important issues still have to be investigated: the assumption of steady recession rate has to be assessed. The effect of the evolving shape of the protrusion on velocity gradients, thus heating rates, has also to be determined using transient (slug) calorimeters of the appropriate geometries.

For each atmosphere, one of the three conditions was selected, and experimental spectra were presented and commented. Their analysis still has to be made using radiation codes (either using PARADE[15] or radiation modeling by Playez[16]) in order to draw conclusions about the state of the gas phase ahead of the surface[17]. In the case of an airstream, Olynick et al.[18] indicate that boundary layer flows over the ablating surface may be, in some conditions, in a chemical nonequilibrium state. As a result, atomic oxygen and nitrogen present at the edge of the boundary layer may survive through the diffusion process to reach the carbon surface. For surface oxidation, reaction coefficients were measured in atomic beam experiments[14]. More experiment is desirable concerning the recent data on nitridation [19]. The relationship of the surface catalytic reactions particularly of N recombination as opposed to direct CN nitridation of the surface significantly alter the surface energy balance in terms of flux and recession rate as shown in the literature [20, 21] using data from Park and Ahn[22] or from Zhluktov and Abe[23]. Park's model has all of the carbon consuming reactions, but does not consider the recombination reactions. Zhluktov and Abe's model has no nitridation reaction, but includes some surface recombination reactions.

The current implementation of laser diagnostic in the VKI plasma facilities[24] is hoped to support the present study, providing space-resolved information on [NO], [N], [O],χ_i,T_{tr} and maybe [CN] ground-state population.

Because radiation of NO and CO in the ultraviolet region is also of interest, and because the improvement of spectral resolution between 320 and 400 nm would help to better characterize the plasma state, the switch from the Ocean Optics spectrometer to a 1 m focal length Jobin-Yvon THR1000MSL, composed of two spherical mirrors and one dispersion element (plane blazed holographic grating, blaze wavelength 750 nm, 1200 grooves/mm) should be done, using the same fiber-based light collection system. The spectrally resolved emission would then be recorded by a CCD camera (Jobin-Yvon ref PCCD2000x800-4) which can monitor emission at multiple wavelengths simultaneously without turning the dispersion grating, scanning the whole spectrum by successive ranges
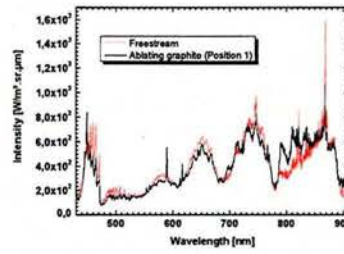
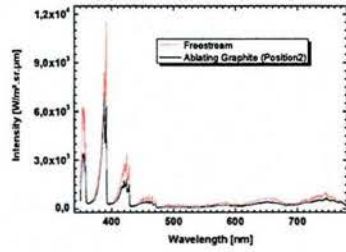(a) Emission spectrum of the nitrogen freestream.
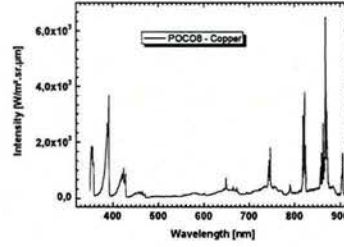
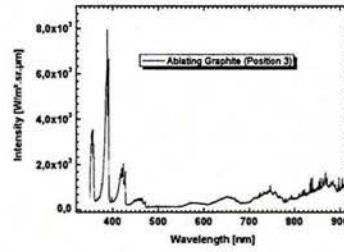(b) Emission spectrum ahead of water-cooled copper surface.
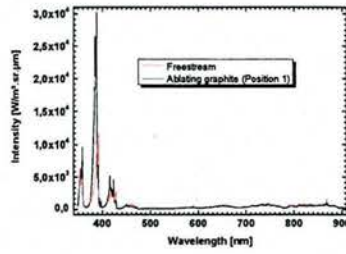
(c) Emission spectrum ahead of ablating graphite.

(d) Emission spectrum ahead of ablating graphite (detail).

(e) Emission spectrum ahead of ablating graphite.

(f) Emission spectrum ahead of ablating graphite.

Figure 1.9: Experimental emission spectra in nitrogen (condition POCO8).

of 200 nm approximately.

Bibliography

[1] Sutton, G. W., "The Initial Development of Ablation Heat Protection: An Historical Perspective," *Journal of Spacecraft and Rockets*, Vol. 19, No. 1, January-February 1982, pp. 3–11.

[2] Vancrayenest, B. and Fletcher, D. G., "Investigation of the Thermochemistry of Ablation of Graphite for Planetary Applications," *Proceedings of the 38th AIAA Thermophysics Conference Meeting and Exhibit*, AIAA 2005-5062, Toronto (Canada), 6-9 June 2005.

[3] Lundell, J. H. and Dickey, R. R., "Ablation of ATJ Graphite at High Temperatures," *AIAA*, Vol. 11, No. 2, Feb. 1973, pp. 216–222.

[4] Wakefield, R. M. and Peterson, D. L., "Graphite Ablation in Combined Convective and Radiative Heating," *Journal of Spacecraft and Rockets*, Vol. 10, No. 2, February 1973, pp. 149–154.

[5] Kolesnikov, A. F., "Extrapolation from High Enthalpy Tests to Flight Based on the Concept of Local Heat Transfer Simulation concept," *Measurements Techniques for High Enthalpy and Plasma Flows*, VKI Lecture Series, Rhode-St-Genèse (Belgium), October 25-29 1999, pp. 8B 1–14.

[6] Fay, J. A. and Riddell, F. R., "Theory of Stagnation Point Heat Transfer in Dissociated Air," *Journal of the Aeronautical Sciences*, Vol. 25, No. 121, 1958, pp. 73–85.

[7] Zoby, E. V. and Sullivan, E. M., "Effects of Corner Radius on Stagnation-Point Velocity Gradients on Blunt Axisymmetric Bodies," *Journal of Spacecraft and Rockets*, Vol. 10, No. 3, October 1966, pp. 1567–1568.

[8] Thömel, J., Rini, P., and Chazot, O., "Sensitivity Analysis of the Local Heat Transfer Simulation for the Application to Thermal Protection Systems," *Proceedings of the 9th AIAA/ASME Joint Thermophysics and Heat Transfer Conference*, No. AIAA-2006-3813, San Francisco (CA), 5-8 June 2006.

[9] Scala, S. M. and Gilbert, L. M., "Sublimation of Graphite at Hypersonic Speeds," *AIAA Journal*, Vol. 3, No. 9, September 1965, pp. 1635–1644.

[10] Touloukian, Y. S., *Thermophysical Properties of Matter: Thermal Radiative Properties - Nonmetallic Solids*, Vol. 8, 1972.

[11] Wilson, R. G. and Spitzer, C. R., "Visible and Near-Infrared Emittance of Ablation Chars and Carbon," *AIAA journal*, Vol. 6, No. 4, April 1968, pp. 665–671.

[12] Raiche, G. A. and Driver, D. M., "Shock Layer Optical Attenuation and Emission Spectroscopy During Arc Jet Testing With Ablative Models," *Proceedings of the AIAA 42nd Aerospace Sciences Meeting & Exhibit*, Reno, Nevada, 5-8 January 2004, AIAA2004-0825.

[13] Park, C. S., Newfield, M. E., Fletcher, D. G., Gökçen, T., and Sharma, S. P., "Spectroscopic Emission Measurements Within the Blunt-Body Shock Layer in an Arcjet Flow," *Journal of Thermophysics and Heat Transfer*, Vol. 12, No. 2, April-June 1998, pp. 190–197.

[14] Park, C., "Effects of Atomic Oxygen on Graphite Ablation," *AIAA Journal*, Vol. 14, No. 11, November 1976, pp. 1640–1642.

[15] Smith, A. J., "ESA PlasmA RAdiation DatabasE (PARADE). Development History, Status, Current Developments and Future Prospects," *ESA SP-533: Radiation of High Temperature Gases in Atmospheric Entry*, edited by B. Warmbein, December 2003, pp. 75–83.

[16] Playez, M., *Titan Atmosphere Plasma Characterization Using Spectroscopic Measurement Techniques*, PhD dissertation, Laboratoire d'Énergétique Moléculaire et Macroscopique, Combustion, École Centrale Paris, June 2006.

[17] Tauber, M. E. and Sutton, K., "Stagnation-Point Radiative Heating Relations for Earth and Mars Entries," *Journal of Spacecraft and Rockets*, Vol. 28, No. 1, January-February 1991, pp. 40–42.

[18] Olynick, D., Chen, Y.-K., and Tauber, M. E., "Aerothermodynamics of the Stardust Sample Return Capsule," *Journal of Spacecraft and Rockets*, Vol. 36, No. 3, May-June 1999, pp. 442–462.

[19] Park, C. and Bogdanoff, D. W., "Shuck Tube Measurement of Coefficient of Reaction of Nitrogen Atoms with Solid Carbon: preliminary results," *Proceedings of the 41st AIAA Aerospace Sciences Meeting and Exhibit*, No. AIAA2003-0158, Reno (NV), 6-9 January 2003.

[20] Havstad, M. A. and Ferencz, R. M., "Comparison of Surface Chemical Kinetic Models for Ablative Reentry of Graphite," *Journal of Thermophysics and Heat Transfer*, Vol. 16, No. 4, October-December 2002, pp. 508–515.

[21] Chen, Y.-K. and Milos, F. S., "Navier-Stokes Solutions with Finite Rate Ablation for Planetary Mission Earth Reentries," *Journal of Spacecraft and Rockets*, Vol. 42, No. 6, November-December 2005, pp. 961–970.

[22] Park, C. and Ahn, H. K., "Stagnation-Point Heat Transfer Rates for Pionner-Venus Probes," *Journal of Thermophysics and Heat Transfer*, Vol. 13, No. 1, January-March 1999, pp. 33–41.

[23] Zhluktov, S. V. and Abe, T., "Viscous Shock-Layer Simulation of Airflow Past Ablating Blunt Body With Carbon Surface," *Journal of Thermophysics and Heat Transfer*, Vol. 13, No. 1, January-March 1999, pp. 50–.

[24] Fletcher, D. G. and Playez, M., "Characterization of Subsonic and Supersonic Plasma Flows," *Proceedings of the 25th AIAA Aerodynamic Measurement Technology and Ground Testing Conference*, No. AIAA-2006-3294, San Francisco (CA), 5-8 June 2006.

WP 2000 – Part 3 Spectroscopic analysis of the boundary layer in front of UHTC samples tested in the Plasmatron facility

Introduction

Emission spectroscopy has been used to identify important gas-phase species that can be directly linked to changes in the material that occur as the surface and in-depth temperature increases. This study was initiated under separate AFOSR funding for testing UHTC samples in ICP plasma facilities. During the test campaign, observers noted significant variation in the plasma emission near the UHTC sample surface, Therefore, further tests of these materials were conducted under the present contract to determine whether or not emission spectroscopy could be used to identify the change in boundary layer emission and to link the emission change to changes in the material. The potential of this approach is demonstrated in the results shown in this report. It is likely that these results, which are unique and are in advance of other plasma facility testing capabilities, can be further developed to provide useful data for the development of re-able thermal protection materials.

Two tests of the UHTC samples were performed in the VKI-Plasmatron facility. The tests conditions are summarized in Table 1.

Test #	Sample #	Date	Static Pressure, mbar	Generator Power, kW	Heat flux, kW/m^2	Dynamic Pressure, Pa	Duration of the test, min	Sample Temperature, C
1	17	18/09/07	100	220	1200	39	3:20	1616
2	7	18/09/07	100	220	1190	38	5:10	1602

Table 1 : Summary of the test conditions

The sample number seventeen, already exposed to the plasma flow during the previous test campaign [1], was firstly used to calibrate the tunnel and then exposed to the plasma flow in the test conditions described in Table 1. This sample was used as a reference, i.e. a sample already exposed to the plasma flow. Following this test the sample number seven was tested in the same test conditions.

Tests Description

The test procedure is similar to the one described in [1]. The test sample is hold in the plasma flow using the sample holder described in [1]. Nevertheless, a short SiC cover was used in the present case. The samples are injected at low power (~110 kW) and the power is increased slowly to its target value in about one minute. The power is decreased slowly at the end of the test to 100 kW, till the temperature surface decreases below 1200C.

The emission of the hot gas present just in front of the surface was collected using the optical system shown in Figure 1. The light emitted by the plasma jet is collected by a spherical mirror, which images the plasma flow after a second reflect on a flat mirror on the entrance of an optical fiber. The captured light is then sent to an Ocean Optics HR4000CG-UV-NIR spectrometer for dispersion and recording of the spectra. The main characteristics of this spectrometer are given in Table 2 .
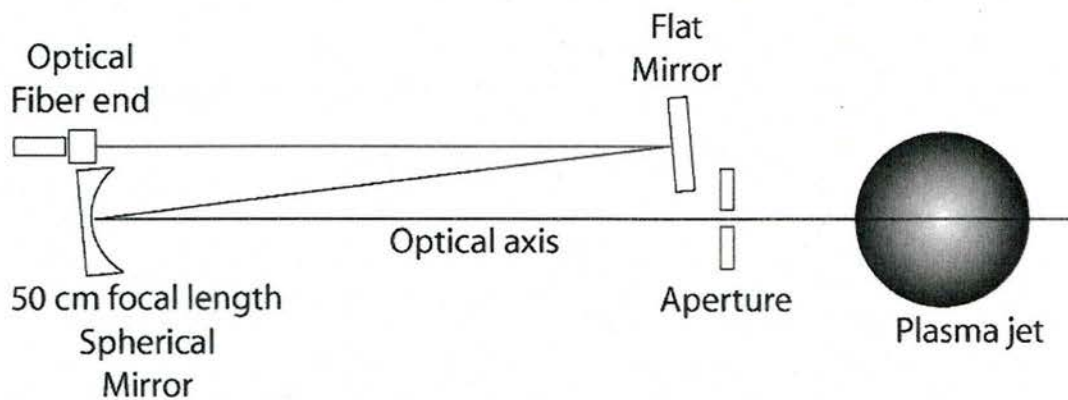
Figure 1 : Plasma emission collection system

Table 2 : characteristics of the Ocean Optics HR4000CG-UV-NIR spectrometer

Wavelength interval:	200-1100 nm
Grating:	300 grooves/mm
F-number:	4
Slit width:	5 μm
Detector:	3648-elements linear silicon CCD array

The collection optics were aligned in a way such that the optical axis was crossing the plasma jet perpendicularly, in the symmetry plane of the sample holder (see Figure 2). The flow contained in a cylinder of 0.4 mm diameter tangent to the surface of the sample was imaged on the entrance of the optical fiber. The optical system was calibrated using a tungsten ribbon lamp (OSRAM ref. WI 17G). The spectral response of the system was

determined for the wavelength interval 350-800 nm where the calibration signal is sufficiently strong to be measured (see Figure 3). The measured spectra are obtained with a wavelength resolution equal to 0.25 nm.
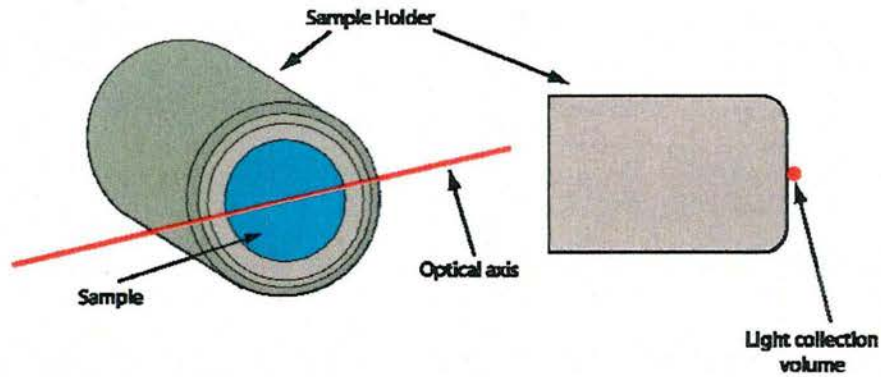

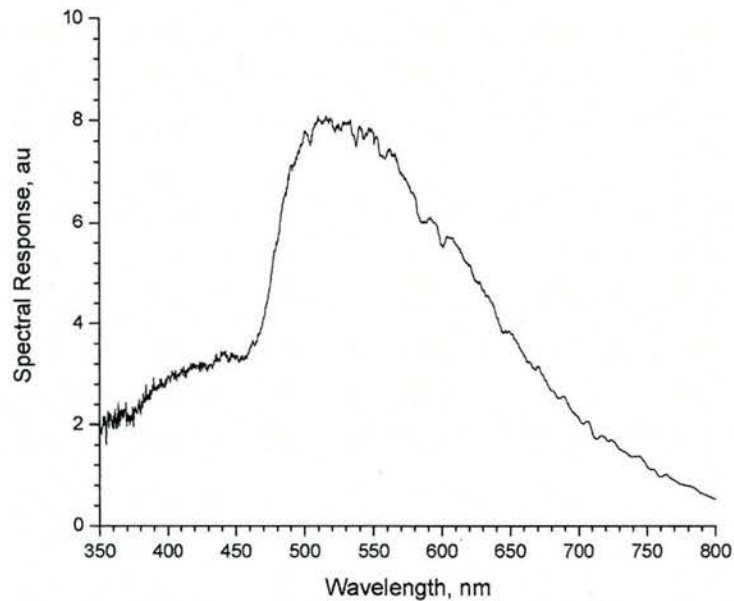**Figure 2 : Definition of the light collection volume**

Figure 3 : Spectral response of the emission spectroscopy system

The temperature of the sample is monitored during the tests using a two-color pyrometer (Raytek Marathon Series MR1SC, Serial #: 46667, lot # 2360430101, Temperature range: 1000-3000°C). The temperature history recorded during the test of the sample number seven is shown in Figure 4.
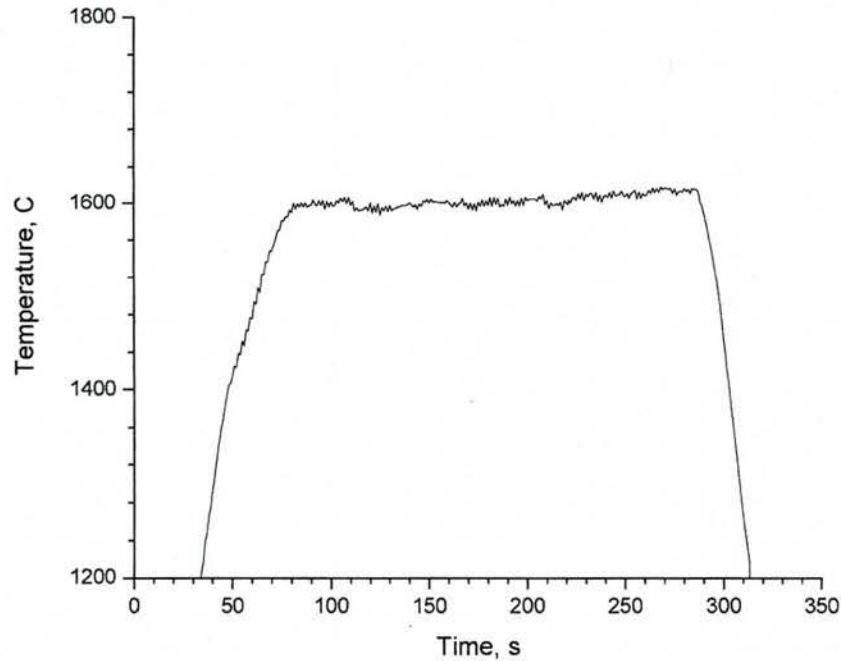
Figure 4 : Temperature history during the second test (sample # 7)

Pictures of the sample holder injected in the plasma flow were taken every second. Two of those pictures are shown in Figure 5. Note the change in color of the gas surrounding the sample holder. This fact was underline in [1]. During the calibration phase performed with sample number 17 a small amount of light with this color was observed but disappeared with time. The tests with the sample number 17 were performed before the test with sample number 7 and the same SiC cover was used for all the runs (calibration and tests). This indicates that the SiC cover does not produce the phenomenon.
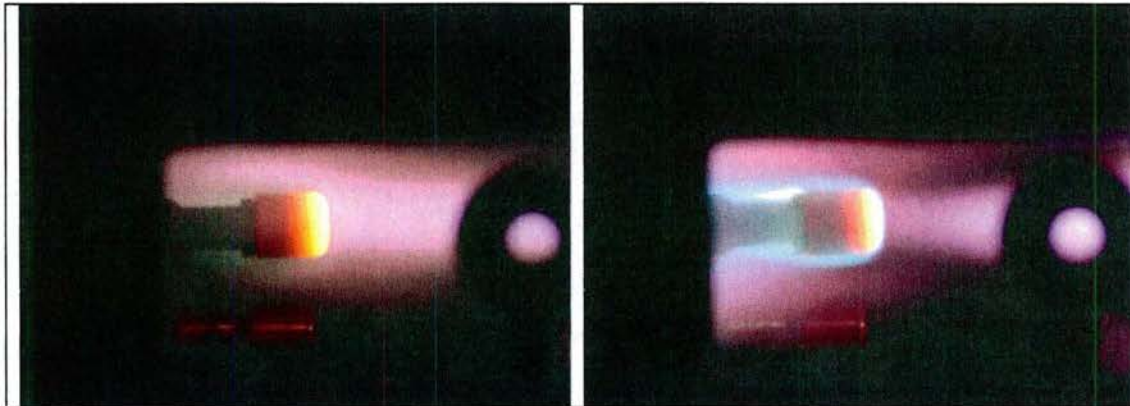
Figure 5 : Pictures of the sample holder during the tests, 55 s after injection of the probe. Sample # 17 is on the right and sample # 7 on the left.

The history of the light emitted at wavelength equal to 506.5 nm is plotted in Figure 6. It shows a strong emission for times between 40 and 150 s.
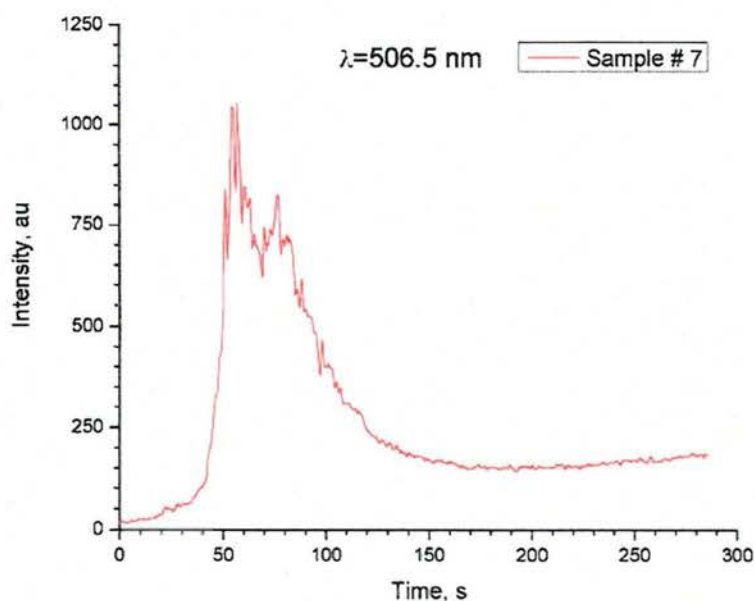
Figure 6 : History of the light emitted at 506.5 nm, second test, sample # 7

After this time period the emission has significantly decreased and varies slowly. This temporal interval corresponds to the end of the temperature increase and the beginning of the steady temperature regime with a temperature varying, between 40 and 80 s, from 1300C to 1600C. The maximum emission is observed at time 55 s. The processed spectrum corresponding to this maximum is plotted in Figure 7. The spectrum measured during the first test and corresponding to the same time after injection of the probe is also plotted in Figure 7. In the same way, the raw data corresponding to those spectra but which shows spectral features over a wider spectral range are plotted in Figure 8. The near infra-red part of the spectra is repeated within ±30 %, thereby showing a reasonable agreement (see
Figure 9). The visible and UV part of the spectra exhibit large differences.

55s after injection of the probe

Sample # 7
Sample # 17

Intensity, au

Wavelength, nm
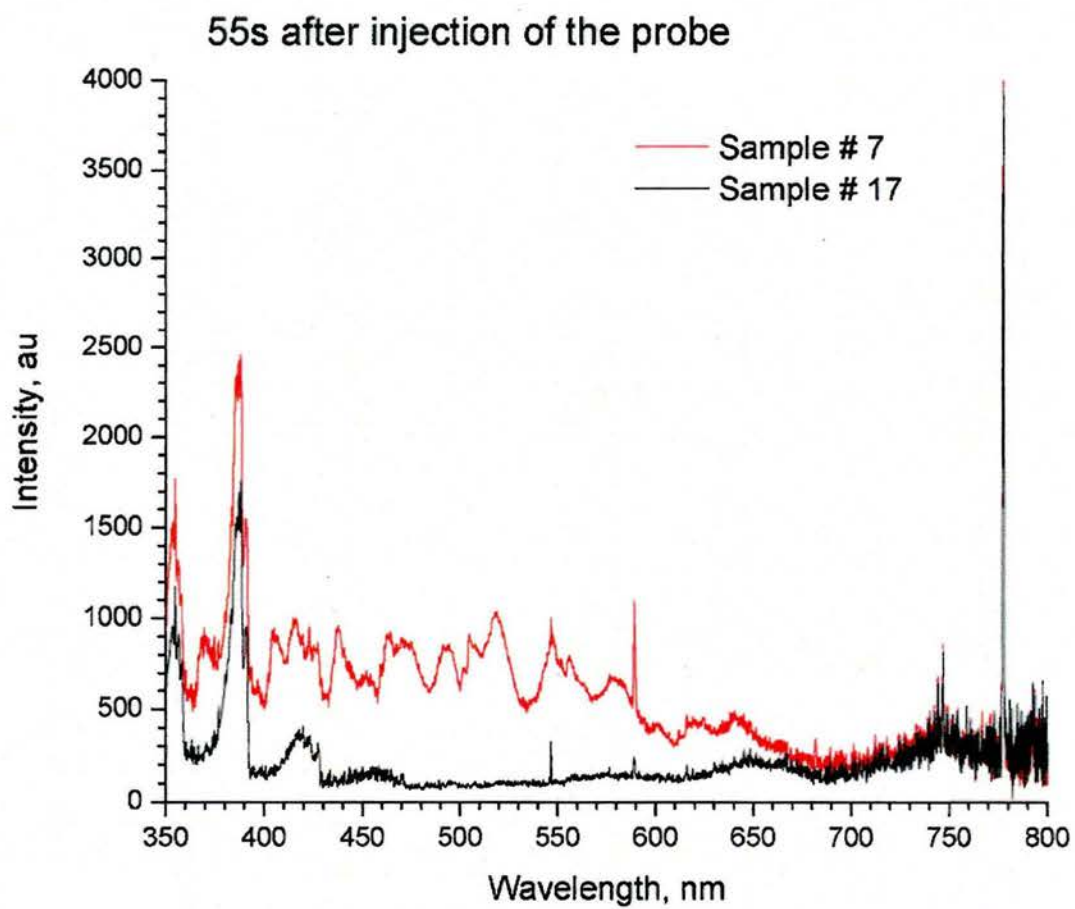
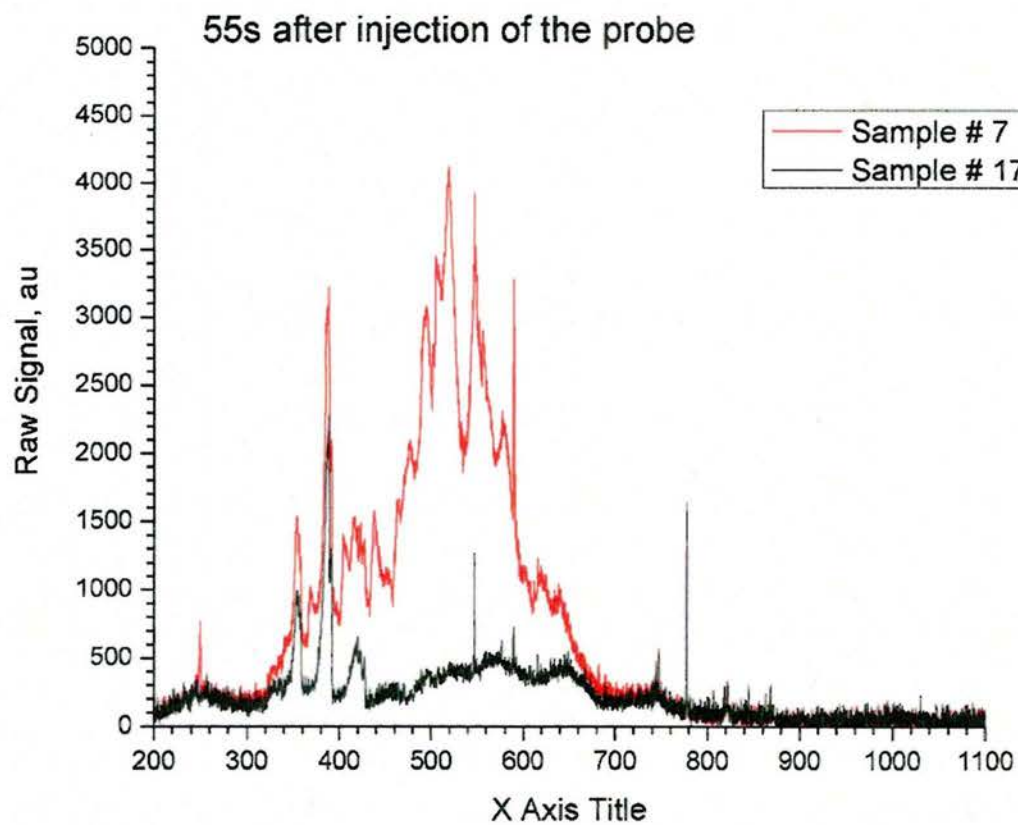Figure 7 : Spectra measured 55 s after the injection of the probe

Figure 8 : Raw data of the spectra measured 55 s after the injection of the probe
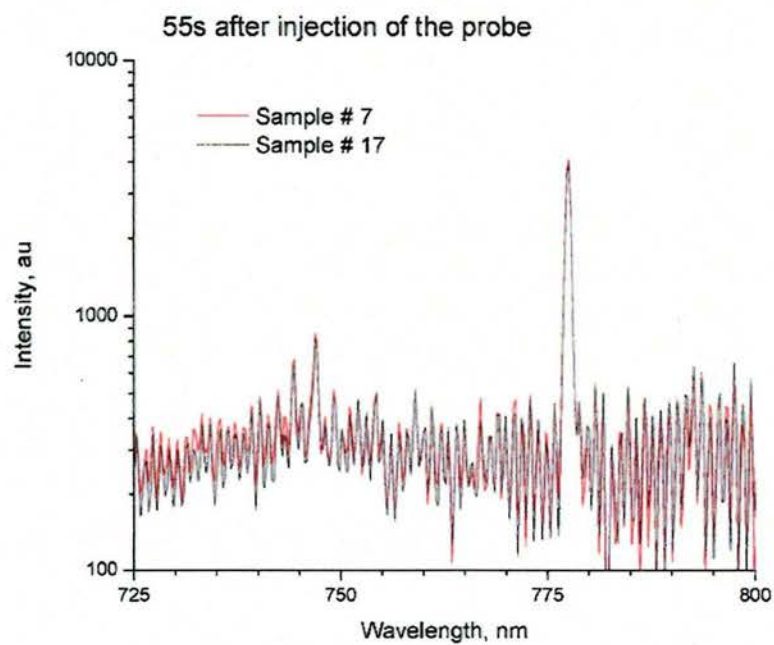

Figure 9 : Repeatability in the near infra-red of the measured spectra between the two tests

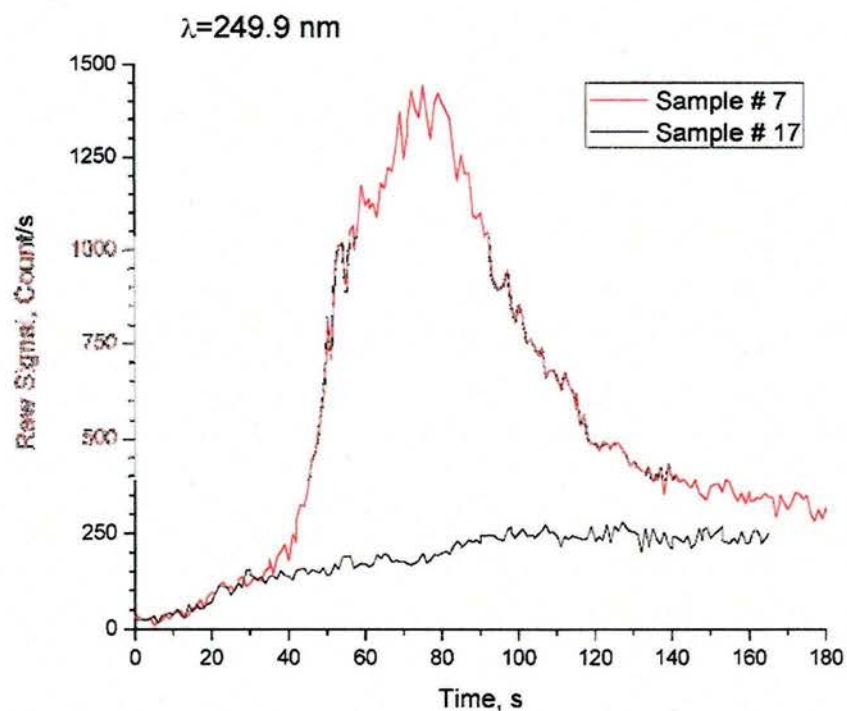The temporal evolution for three wavelengths: 249.9, 506.5 and 777.5 nm is plotted in figures Figure 10Figure 12.

Figure 10 : Temporal evolution of the measured raw signal at 249.9 nm
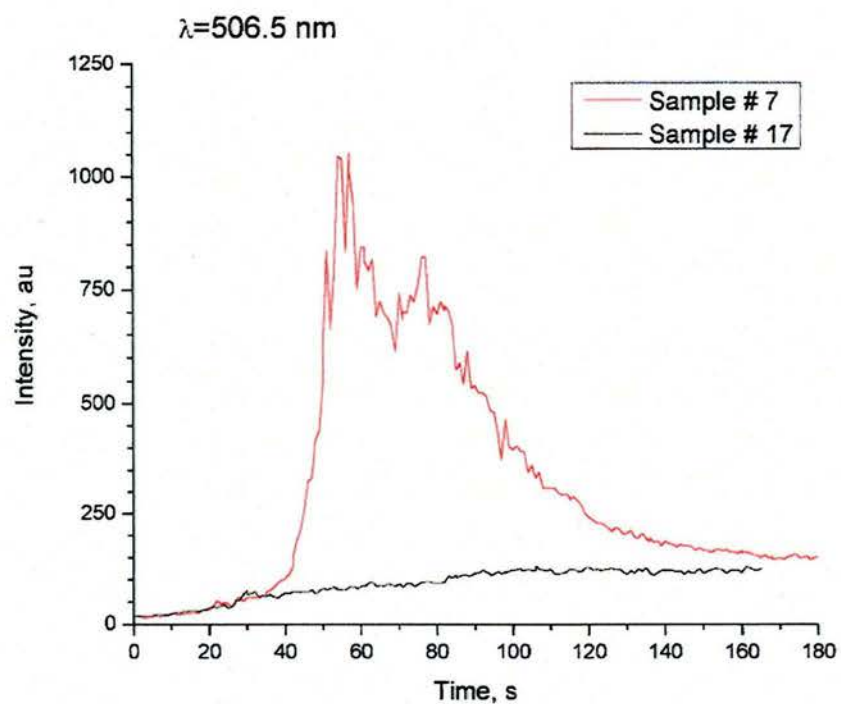
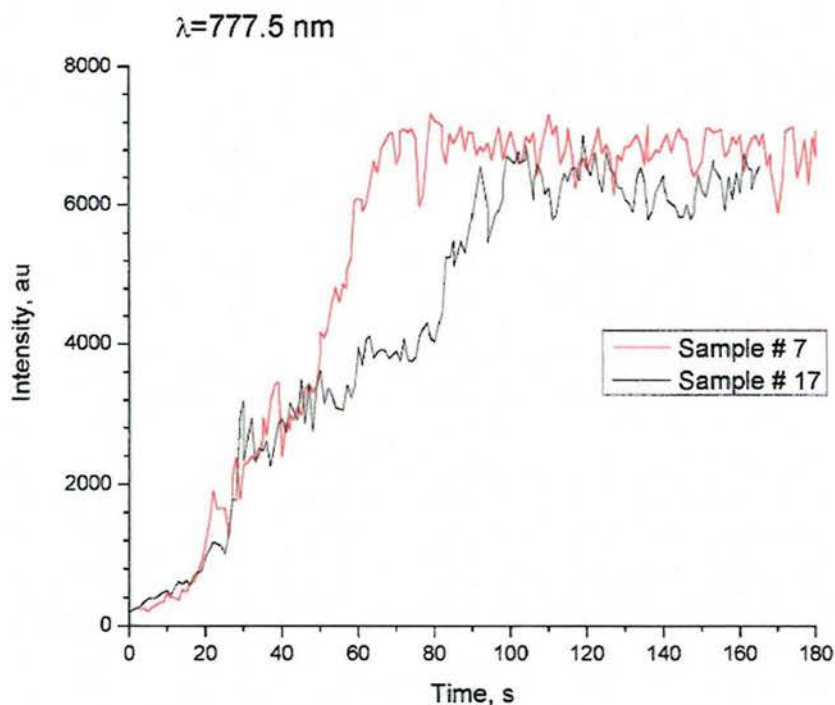Figure 11 : Temporal evolution of the measured intensity at 506.5 nm

Figure 12 : Temporal evolution of the measured intensity at 777.5 nm

The intensity of Figure 10 corresponds to the peak intensity of a spectral feature identified as an unresolved atomic doublet emitted by boron ($2s^2 3s \ ^2S_{1/2} \rightarrow 2s^2 2p \ ^2P°_{1/2,3/2}$). The intensity plotted in Figure 11 corresponds to the band head of a molecular system giving a measurable signal for wavelength values between 300 and 700 nm. This system is thought to be emitted by boron oxides, this would be consistent with the measured atomic boron line. The third temporal evolution is plotted for a wavelength corresponding to the unresolved triplet of atomic oxygen ($2s^2 2p^3(^4S°)3p \ ^5P_{1,2,3} \rightarrow 2s^2 2p^3(^4S°)3s \ ^5S°_2$). While in the case of atomic oxygen, only small deviations are observed between the two tests, the presence of boron is only measured for times between 30 seconds and 160 seconds where the two measurements converge to close the same values. The spectra of the two samples for times equal to 30 and 160 s are shown in Figure 13 and Figure 14.
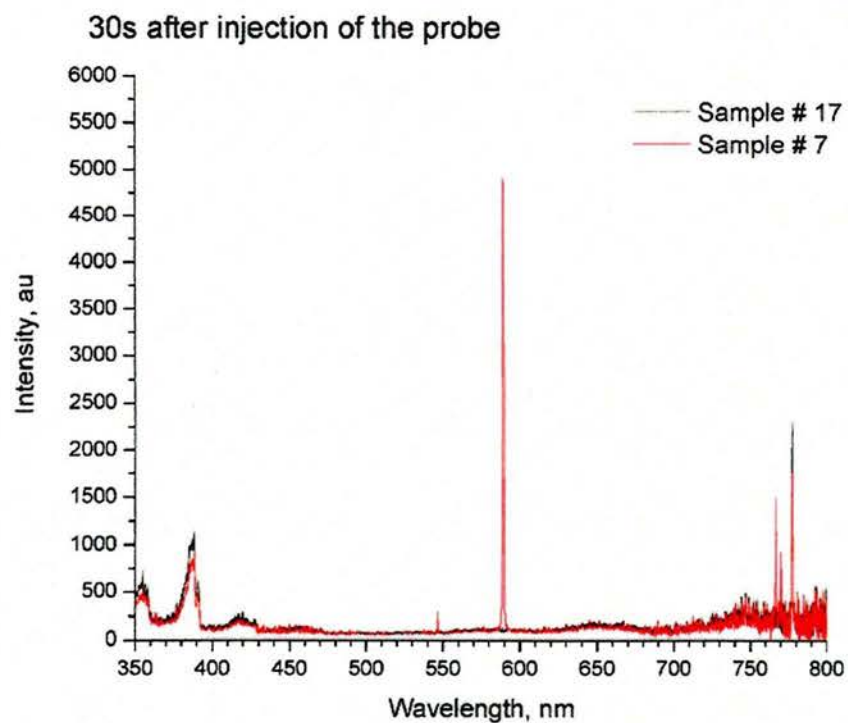
30s after injection of the probe

Figure 13: Spectra measured 30 s after the injection of the probe
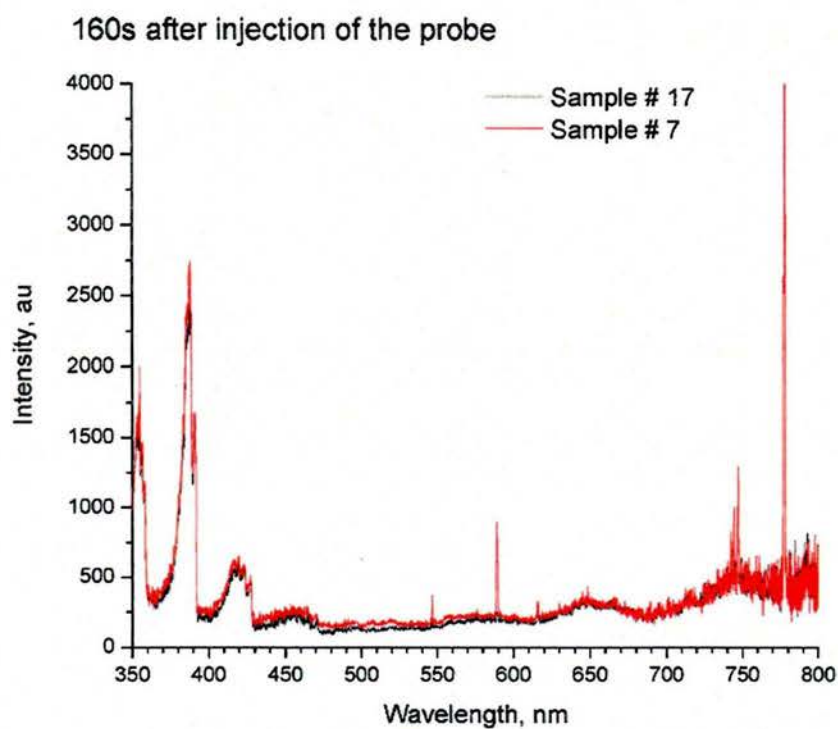
160s after injection of the probe

Figure 14 : Spectra measured 160 s after the injection of the probe

An atomic line at 589 nm can be seen in these spectra. This line can be attributed to sodium ($2p^63p$ $^2P^{\circ}_{3/2,1/2} \rightarrow 2p^63s$ $^2S_{1/2}$ doublet) . The temporal evolution of this spectral feature is plotted in Figure 15. Large fluctuations of the emitted line are observed. Furthermore, the emission does not decrease to the value of the sample number seventeen. In Figure 13, two other spectral lines at 766.7 and 769.9 nm are also present in the test with sample number seven, but not with sample number seventeen. The evolution of the emission at these wavelengths is presented in Figure 16 and Figure 17. They present the same temporal behavior and have a behavior similar to the one observed in Figure 15 for times below 50 s. These lines can be attributed to tungsten but the low spectral resolution of the measurements does not allow determining with certainty the nature of the element.
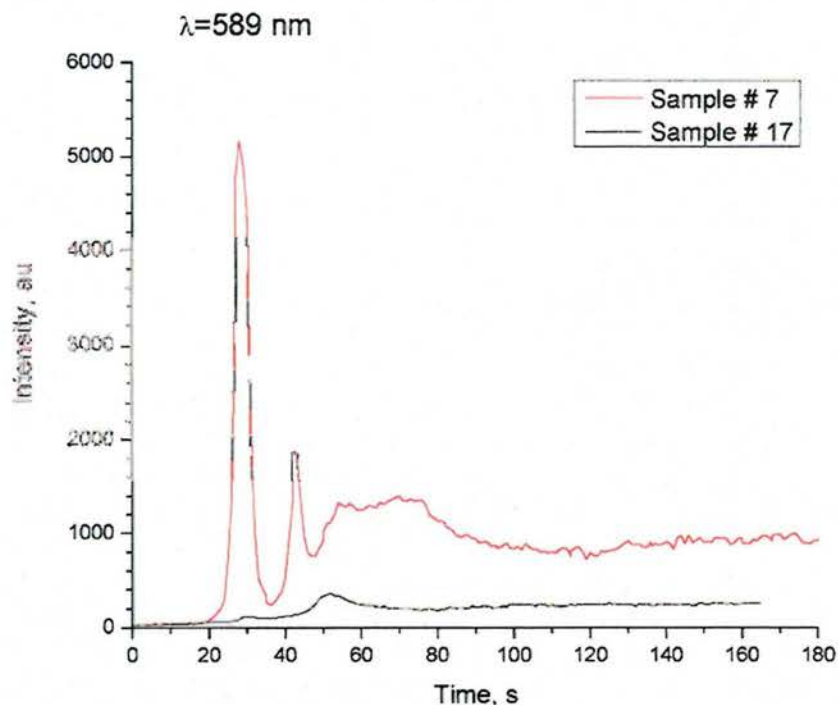

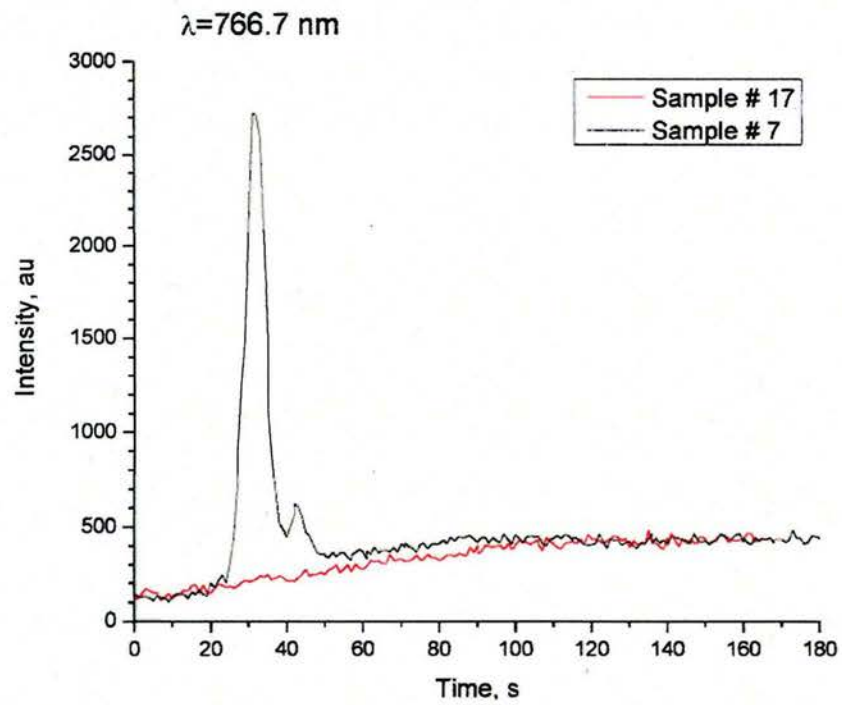**Figure 15 : Temporal evolution of the measured intensity at 589 nm**

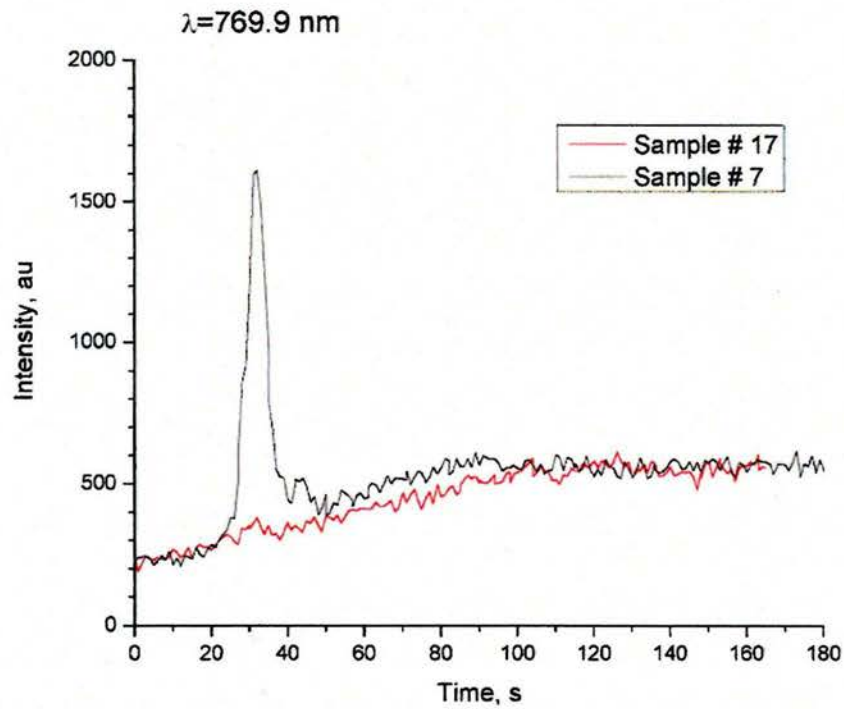**Figure 16 : Temporal evolution of the measured intensity at 766.7 nm**

Figure 17 : Temporal evolution of the measured intensity at 769.9 nm

Conclusion

Emission spectroscopy measurements performed in front of UHTC samples tested in the VKI-Plasmatron facility were presented. Two samples were tested. A sample already exposed to the plasma flow and a virgin sample. The emission spectra measured in front of those two samples were compared and large differences were observed in the visible and UV part of the spectra. The temporal evolution of different spectral features was presented and showed the transient behavior of the emission. The spectral features were attributed to boron, boron monoxide, sodium and tungsten.

References

[1] C. Asma, J. Thoemel, P. Collin and D. Fletcher, "Testing of UHTC Samples in the VKI Plasmatron", Von Karman Institute for Fluid Dynamics Contract Report CR2006-27